

# Control of cell–cell forces and collective cell dynamics by the intercellular adhesome

Elsa Bazellères<sup>1</sup>, Vito Conte<sup>1</sup>, Alberto Elosegui-Artola<sup>1</sup>, Xavier Serra-Picamal<sup>1</sup>, María Bintanel-Morcillo<sup>1</sup>, Pere Roca-Cusachs<sup>1,2</sup>, José J. Muñoz<sup>3</sup>, Marta Sales-Pardo<sup>4</sup>, Roger Guimerà<sup>4,5</sup> and Xavier Trepat<sup>1,2,5,6</sup>

**Dynamics of epithelial tissues determine key processes in development, tissue healing and cancer invasion. These processes are critically influenced by cell–cell adhesion forces. However, the identity of the proteins that resist and transmit forces at cell–cell junctions remains unclear, and how these proteins control tissue dynamics is largely unknown. Here we provide a systematic study of the interplay between cell–cell adhesion proteins, intercellular forces and epithelial tissue dynamics. We show that collective cellular responses to selective perturbations of the intercellular adhesome conform to three mechanical phenotypes. These phenotypes are controlled by different molecular modules and characterized by distinct relationships between cellular kinematics and intercellular forces. We show that these forces and their rates can be predicted by the concentrations of cadherins and catenins. Unexpectedly, we identified different mechanical roles for P-cadherin and E-cadherin; whereas P-cadherin predicts levels of intercellular force, E-cadherin predicts the rate at which intercellular force builds up.**

The homeostasis of epithelial tissues and its disruption during disease are enabled by collective cellular processes such as growth, migration and remodelling<sup>1–3</sup>. Each of these collective processes has long been known to be critically influenced by cell–cell adhesion complexes. To a significant extent, this critical influence has its mechanistic origin in the ability of cell–cell adhesions to transmit physical forces<sup>4–13</sup>.

Force transmission through intercellular junctions is traditionally attributed to adherens junctions, which provide a physical connection between the actomyosin cytoskeleton and transmembrane proteins of the cadherin superfamily<sup>14–17</sup>. However, the identity of the molecules that transmit physical forces in adherens junctions remains controversial. For example, epithelial cells often express several cadherin isoforms<sup>18,19</sup>, including E-cadherin, N-cadherin and P-cadherin<sup>18,19</sup>. The balance in the expression of these different cadherins is known to be essential to maintain tissue homeostasis<sup>18–23</sup> but the extent to which each classical cadherin is involved in force transmission is unknown. Moreover, the network of proteins that provides a physical connection between cadherins and the cytoskeleton is also incomplete.  $\beta$ -catenin and  $\alpha$ -catenin link cadherins and F-actin<sup>24</sup> but other proteins such as ZO-1, vinculin and LIMA1 have also been proposed to contribute to force transmission<sup>17,25,26</sup>.

Besides adherens junctions, the actomyosin cytoskeleton of adjacent cells is also connected through tight junctions, which comprise transmembrane receptors such as claudins, occludin and JAM-A, as well as intracellular linkers such as ZO-1, ZO-2 and ZO-3 (ref. 27). Tight junctions are typically associated with epithelial sealing rather than force transmission, but no experimental evidence has so far ruled out the ability of tight junctions to resist and transmit physical forces. In addition to the actin cytoskeleton, forces within epithelial sheets have also been proposed to be transmitted by intermediate filaments within cells and by desmosomes between cells<sup>28–30</sup>. Finally, gap junctions, which play a major role in controlling the intercellular transit of ions and small solutes between cells, have been shown to be mechanosensitive<sup>31</sup>, thus raising the possibility that they might play a mechanical role in epithelial tissue dynamics.

Here we used micropatterned sheets of epithelial cells as a model system to study the interplay between intercellular adhesion proteins, physical forces and tissue dynamics. We designed a minimal custom library of validated short interfering RNAs (siRNAs) targeting the main molecular components of the intercellular adhesome. For each siRNA perturbation we measured cellular velocities and deformation rates, as well as intercellular, intracellular and extracellular forces. Using unsupervised clustering analysis, we identified systematic

<sup>1</sup>Institute for Bioengineering of Catalonia, Barcelona 08028, Spain. <sup>2</sup>Unitat de Biofísica i Bioenginyeria, Facultat de Medicina, Universitat de Barcelona, and CIBERES, Barcelona 08036, Spain. <sup>3</sup>Laboratori de Càlcul Numèric, Department of Applied Mathematics III, Universitat Politècnica de Catalunya, Barcelona 08036, Spain.

<sup>4</sup>Departament d'Enginyeria Química, Universitat Rovira i Virgili, Tarragona 43007, Catalonia, Spain. <sup>5</sup>Institució Catalana de Recerca i Estudis Avançats (ICREA), Barcelona 08010, Spain.

<sup>6</sup>Correspondence should be addressed to X.T. (e-mail: [xtrepat@ibecbarcelona.eu](mailto:xtrepat@ibecbarcelona.eu))

relationships between these physical properties and molecular control modules within the adhesome. Using a cross-validation analysis we established the ability of intercellular adhesion proteins to quantitatively predict tissue dynamics.

## RESULTS

### Intercellular cohesiveness increases with monolayer expansion

We developed an assay to measure in parallel the epithelial dynamics of multiple expanding monolayers (Fig. 1a,b). Using soft lithography, thin polydimethylsiloxane (PDMS) membranes with a rectangular opening were fabricated and deposited on top of a collagen-I-coated polyacrylamide gel substrate<sup>13,32</sup>. We then seeded normal breast epithelial cells (MCF10A) and allowed them to adhere and spread until they formed a confluent monolayer. After 5 h of culture, F-actin was largely cortical but the monolayer was not cohesive; cadherins, catenins and ZO-1 were either fully cytoplasmic or weakly localized at the lateral cell–cell contact areas (Fig. 1c,e).

On lifting the PDMS membrane, the monolayer expanded towards the available gel surface and, after 6 h of migration, its area had increased by ~27% (Fig. 2a,b,i and Supplementary Video 1). At this point, cadherins, catenins and ZO-1 progressively accumulated at the cell cortex, and this accumulation was more pronounced in the central region of the monolayer (Fig. 1d,f). Thus, as the monolayer expanded it increased its structural cohesiveness through recruitment of cell–cell adhesion proteins to the cell cortex.

### As the monolayer increases its cohesiveness, cell migration slows down and intercellular forces build up

We next studied how the increase in monolayer cohesiveness was paralleled by changes in physical properties of the constituent cells, including cellular velocities, intercellular and intracellular forces, and traction forces at the cell–substrate interface. To map cell velocities during monolayer expansion we used particle imaging velocimetry<sup>13</sup>. Velocity fields showed large spatial heterogeneities that spanned several cell diameters (Fig. 2c,d and Supplementary Video 2)<sup>6,13</sup>. Despite these large fluctuations, cells moved predominantly away from the initial pattern and, as the monolayer expanded, the average cell velocity decreased (Fig. 2j).

Simultaneously with cell velocities we measured traction forces exerted by cells on the underlying substrate. From the onset of monolayer expansion, traction forces exhibited a punctate spatial distribution characterized by rapid fluctuations in magnitude and direction (Fig. 2e,f and Supplementary Video 2). To assess the total traction exerted by cells in the monolayer we computed the strain energy density ( $U$ ) transferred by cells to the gel.  $U$  increased with time and tended to saturate after 300 min (Fig. 2k), indicating that cells approached a mechanical steady state.

We next examined whether the accumulation of adhesion proteins at intercellular contacts was paralleled by an increase in cell–cell forces. To address this question we used monolayer stress microscopy (MSM), which computes the state of mechanical stress (force per unit cross-sectional area) everywhere within the cell sheet<sup>6,13,33–35</sup>. MSM is based on the principle that traction forces applied at the cell–gel interface must be balanced by intracellular and intercellular forces<sup>36–39</sup>. For simplicity, we mainly focused on  $\sigma_{xx}$ , the stress component in the direction of expansion of the monolayer, and referred to it indistinctly

as monolayer tension or intercellular tension (see Supplementary Note for other stress components). Monolayer tension exhibited well-known features of expanding epithelial sheets including dynamic heterogeneities and supracellular fluctuations (Fig. 2g,h and Supplementary Video 2)<sup>6,13,33</sup>. Similarly to the case of traction forces, all components of the stress tensor increased monotonically with time and tended to plateau as expansion slowed down (Fig. 2l).

Taken together, our data put forward the following scenario. As the monolayer expands, it matures its intercellular adhesions with a cortical recruitment of cadherins, catenins and ZO-1. These structural changes are paralleled by a progressive decrease in cell velocity, and a pronounced increase in cell–substrate forces and intercellular tension.

### Downregulation of cell–cell adhesion proteins alters cell velocities, cell tractions and intercellular tension

We next sought to identify what proteins are involved in the regulation and transmission of monolayer tension. To do so, we designed a minimal siRNA library to selectively knock down the main molecular players of the intercellular adhesome (Supplementary Fig. 1a). Specifically, we targeted key transmembrane proteins associated with adherens junctions, tight junctions, desmosomes and gap junctions. In addition, we targeted a subset of cytoplasmic proteins that have been shown or proposed to be involved in linking these transmembrane proteins to the actin and intermediate filament cytoskeleton.

To effectively knock down genes coding for intercellular adhesion proteins we transfected cells with a pool of 3 distinct siRNAs and carried out monolayer expansion experiments 5 days later. All siRNA pools efficiently downregulated their respective target genes with an average messenger RNA knockdown of  $81\% \pm 11\%$  (mean  $\pm$  s.e.m.; Supplementary Fig. 1b).

Representative maps of cell velocity ( $V_x$ ), traction force ( $T_x$ ) and intercellular tension ( $\sigma_{xx}$ ) for a subset of siRNAs are shown in Figs 3 and 4 (see also Supplementary Figs 2–7 for a complete set of representative experiments). These maps confirm previous studies showing that downregulation of E-cadherin or N-cadherin has no impact on cellular velocities (Fig. 3b and Supplementary Fig. 2)<sup>21,40</sup>. Our data show, further, that loss of function of these cadherins does not influence the transmission of intercellular tension (Fig. 3b and Supplementary Fig. 2 and Supplementary Video 3). In contrast, knocking down P-cadherin led to monolayer dissociation, an increase in cell velocity and a sharp drop in monolayer tension (Fig. 3c). Similarly, downregulation of catenins led to faster monolayer expansion and lower intercellular tension (Fig. 3d–f and Supplementary Fig. 3). Knockdown of LIMA1 and DDR1 did not impact significantly monolayer dynamics (Supplementary Fig. 4). Together, these data suggest that P-cadherin associates with catenins to mediate intercellular force transmission in MCF10A cells.

siRNAs targeting desmosomes, tight junctions and gap junctions also altered cellular velocities, tractions and tensions (Fig. 4a–f and Supplementary Figs 5–7). Downregulation of the tight junction proteins ZO-1 and ZO-3 led to marked but opposite changes in monolayer mechanics (Fig. 4c,d). Downregulation of desmosomal proteins caused minor changes in monolayer forces and kinematics with the exception of DSC3, which slowed down cell migration (Fig. 4e and Supplementary Fig. 7). Finally, siRNAs targeting the gap junction protein CX43 caused a weak decrease in traction forces

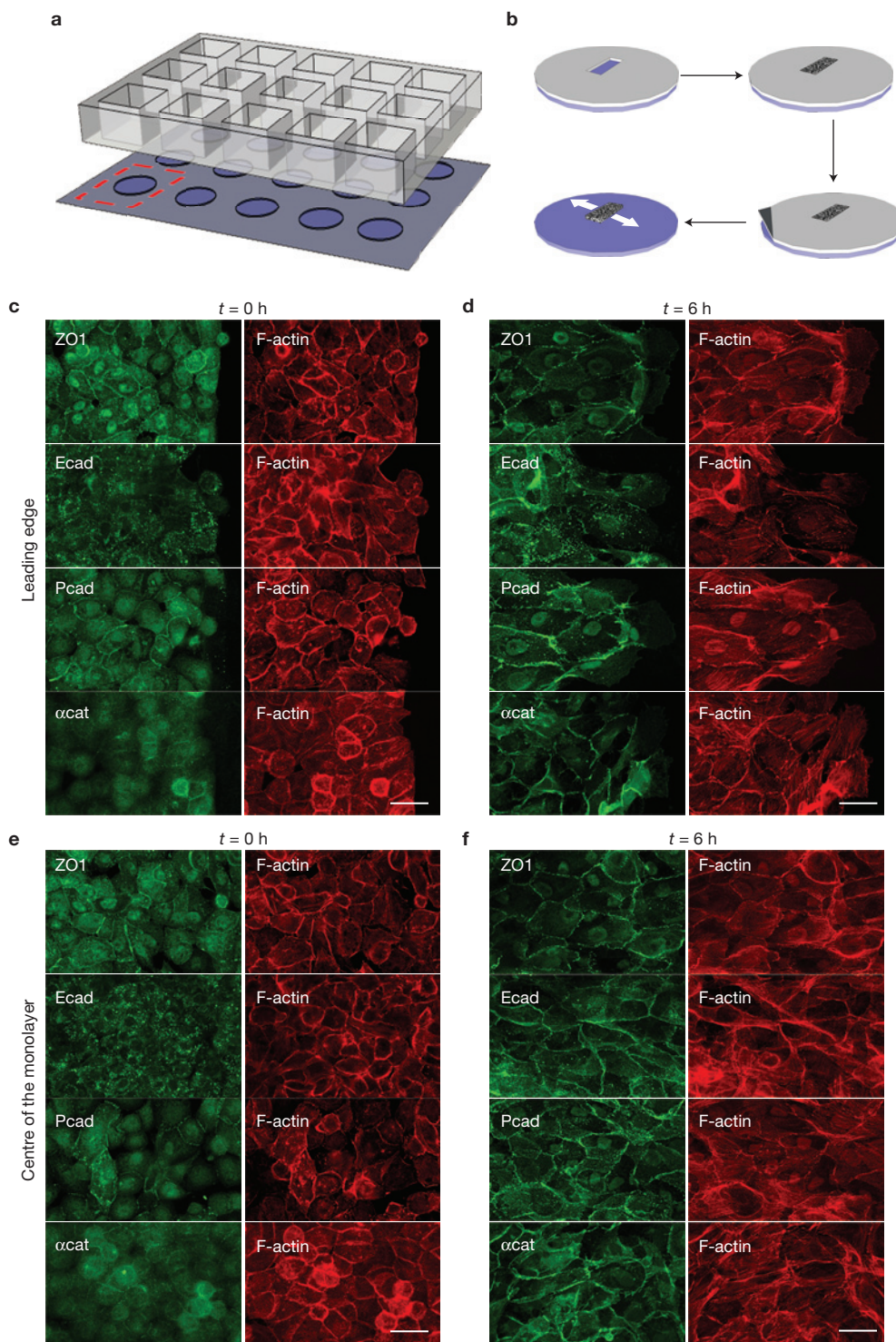


**Figure 1** Intercellular cohesiveness increases with monolayer expansion. (a,b) Scheme of the experimental set-up. (a) A large glass slide was attached to a custom-made PDMS frame containing 15 openings that served as individual wells. Each well contained a collagen-I-coated micropatterned gel. (b) A PDMS membrane with a rectangular opening was deposited on top of each

polyacrylamide gel. Next, cells were seeded on top of each gel and allowed to adhere. After 5 h, the PDMS membranes were removed. (c–f) Localization of ZO-1, E-cadherin, P-cadherin,  $\alpha$ -catenin and F-actin at the leading edge (c,d) and centre (e,f) of the monolayer immediately after removing the PDMS membranes (c,e) and after 6 hours of expansion (d,f). Scale bars, 20  $\mu$ m.

and intercellular tension (Fig. 4f). Thus, proteins associated with junctional complexes other than adherens junctions also seem to be involved in the regulation of monolayer dynamics.

We next focused on the time evolution of monolayer dynamics in response to siRNAs. For each time point, we averaged maps of each physical property across space and over all experimental

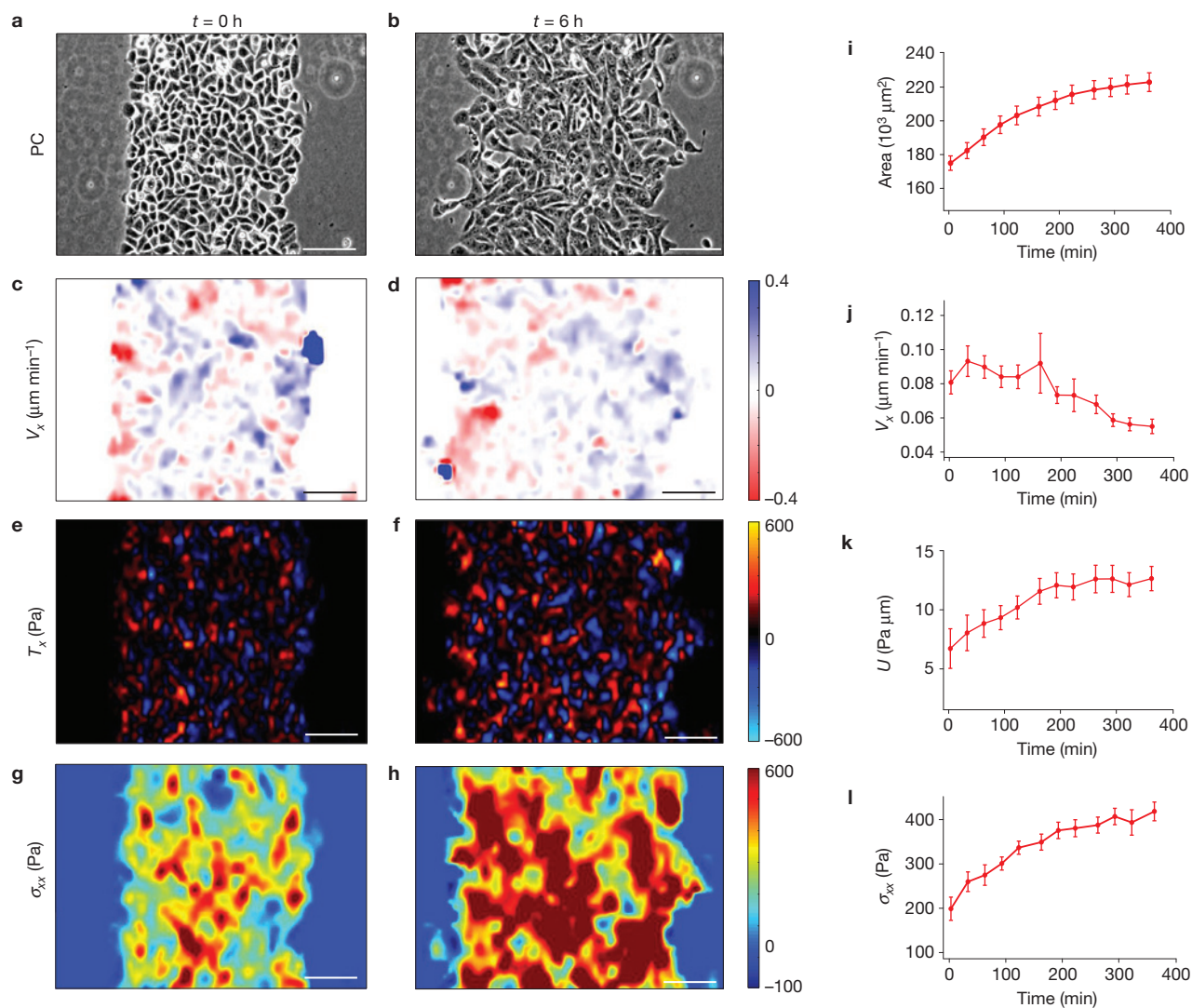


**Figure 2** As the monolayer increases its cohesiveness, cell migration slows down and physical forces build up. (a–h) Phase-contrast (PC) images (a,b), maps of cell velocities (c,d), maps of traction forces (e,f), and maps of monolayer tension (g,h) at  $t = 0$  h (a,c,e,g) and  $t = 6$  h (b,d,f,h).

(i–l) Time evolution of monolayer area (i), cell velocity (j), strain energy density (k), and monolayer tension (l). Scale bars,  $100 \mu\text{m}$ . Data are presented as mean  $\pm$  s.e.m. ( $n = 13$  independent cell monolayers assessed over 10 experiments).

repeats (see Methods and Supplementary Note). The time evolution of these averages showed that the global trends of control experiments were generally conserved under siRNA perturbations but with clear exceptions (Figs 3g–j and 4g–j and Supplementary Fig. 8). For example, the general tendency of intercellular forces to increase with monolayer expansion was disrupted by a number of siRNAs—for example, p120 siRNA,  $\beta$ cat siRNA and Pcad siRNA (Fig. 3j). Taken together, our data indicate that proteins from distinct junctional complexes alter monolayer kinematics and forces, as well as the time evolution of these physical properties.

### Forces and kinematics are anticorrelated

The diversity of responses to siRNAs prompted us to study systematically the mechanical phenotypes explored by cell monolayers. To do so, we first examined whether physical properties that define tissue dynamics are linked through universal relationships or whether they

are generally uncorrelated. We began by identifying a minimal set of properties that fully captured the diversity of observed mechanical phenotypes (Supplementary Note). We selected the following properties, averaged over time, space and experimental repeats: cell velocity  $V_x$ , cell deformation rate  $\dot{\epsilon}_{xx}$ , increase in monolayer area  $\Delta A$ , strain energy density transferred by cells to the substrate  $U$ , and maximum shear stress  $\sigma_s$ . In addition, to capture monolayer tension to first order in time we considered the average value of  $\sigma_{xx}$  at the end of the experiment ( $\sigma_{xx}^f$ ) and the average slope of its time evolution ( $\sigma_{xx}^f$ ). In this way, we were able to summarize our data in an  $m \times n$  matrix comprising  $m$  siRNA perturbations, and  $n$  physical properties ( $m = 21$ ,  $n = 7$ ). From this data matrix, we computed a matrix  $Z$ , in which each element  $Z_{ij}$  (element located on row  $i$  and column  $j$ ) contains the  $z$ -score of the physical property  $j$  in response to a siRNA perturbation  $i$  (Fig. 5a; see Methods for a description of  $z$ -score calculations).

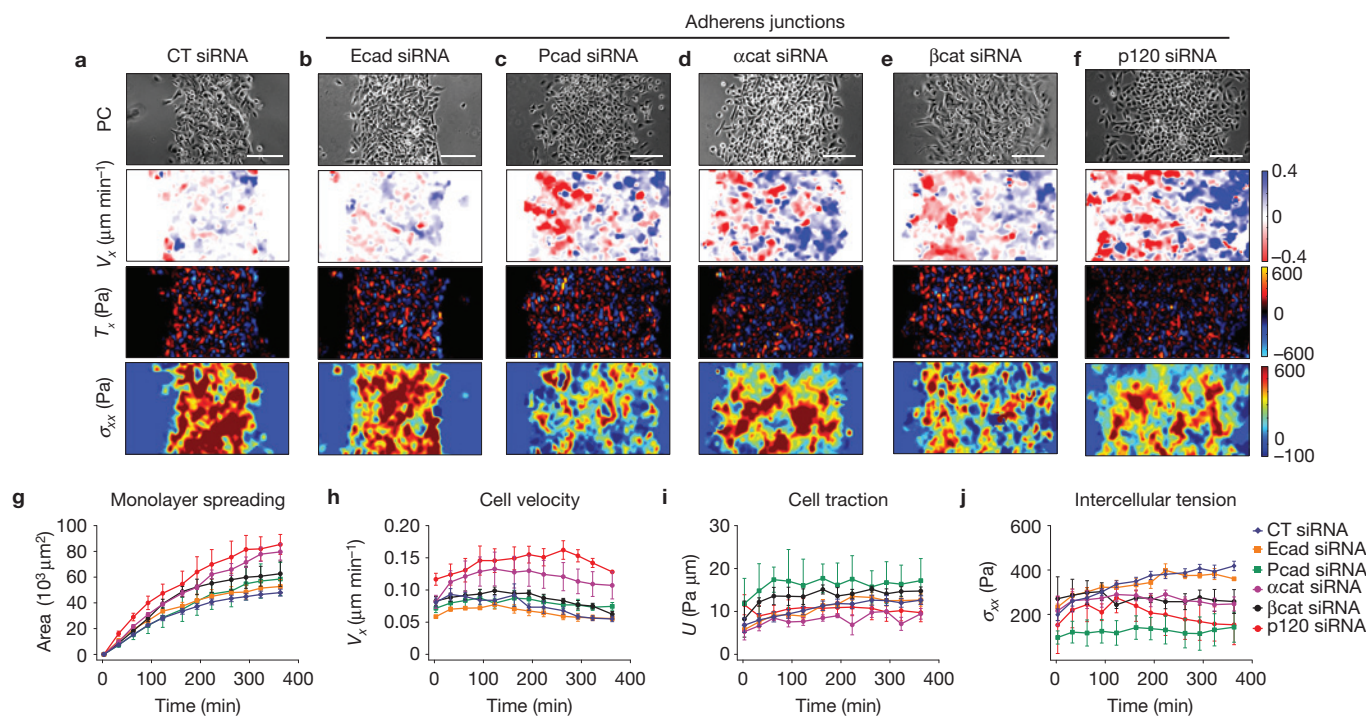


**Figure 3** Downregulation of adherens junctions alters monolayer dynamics. (a–f) Representative maps showing the effect of siRNAs on monolayer dynamics after 8 h of expansion. For each siRNA, phase-contrast images (first row), monolayer velocity (second row), traction force (third row), and intercellular tension (fourth row) are shown. Columns show the control case (a) and selected siRNAs targeting adherens junctions (b–f). Additional time points and siRNA perturbations are shown in Supplementary Figs 2–4. (g–j) Time evolution of monolayer area (shown as the increase from the initial area; g), cell velocity

(h), strain energy density (i), and intercellular tension (j) for the control case and siRNAs shown in b–f. The time evolution of physical properties in response to all siRNAs is shown in Supplementary Fig. 8. Scale bars, 100  $\mu\text{m}$ . Data are presented as mean  $\pm$  s.e.m.  $n=13$  independent cell monolayers (CT siRNA),  $n=4$  independent cell monolayers ( $\alpha$ cat siRNA, Pcad siRNA, p120 siRNA),  $n=3$  independent cell monolayers (Ecad siRNA,  $\beta$ cat siRNA); monolayers were assessed over 10 experiments (CT siRNA), 3 experiments ( $\alpha$ cat siRNA), 2 experiments (Pcad siRNA, p120 siRNA, Ecad siRNA,  $\beta$ cat siRNA).

We then computed a cross-correlation between  $z$ -scores of each possible pair of physical variables (that is, correlations between columns in Fig. 5a). Among the  $m$  siRNA perturbations, we considered only the subset of  $q$  perturbations having at least one physical property that differed from the control by more than two standard deviations ( $q=12$ ). Correlation analysis yielded an  $n \times n$  symmetric matrix  $C_p$ , where each element  $C_{pi}$  indicates the correlation between physical properties  $i$  and  $j$  (Fig. 5b). We then used an unsupervised algorithm<sup>41</sup> to cluster together the physical properties with highest correlation (Supplementary Note).

Our analysis unveiled two clusters of highly correlated physical properties (Fig. 5b). The first cluster comprises physical properties that describe monolayer kinematics, namely, velocity, increase in monolayer area, and deformation rate. The second cluster comprises physical variables that describe monolayer forces, namely, the strain energy density, the maximum shear stress, monolayer tension at the end of the experiment and the build-up rate of monolayer tension.

### siRNA perturbations can be sorted according to their impact on physical properties

We next examined what siRNA perturbations had a similar impact on physical properties. To address this question, we computed correlations between pairs of siRNA perturbations (that is, correlations between rows in Fig. 5a). The resulting correlation matrix

is a  $q \times q$  symmetric matrix  $C_s$ , where each element  $C_{sj}$  indicates the correlation between siRNA perturbations  $i$  and  $j$  (Fig. 5c).

Our unsupervised algorithm identified three clusters of siRNAs as regards their impact on physical properties (Fig. 5c). The first cluster includes only the siRNAs targeting ZO-1, which showed a correlation profile that was clearly distinct from any other siRNA perturbation. The second cluster comprises siRNAs targeting all adherens junction proteins as well as the tight junction protein occludin. The third cluster includes siRNAs targeting proteins from diverse intercellular complexes including the tight junction proteins CLDN8, ZO-3 and JAM-A, the gap junction protein CX43, and the desmosomal protein DSC3.

### Cell monolayers explore distinct mechanical phenotypes

We next used the unsupervised clustering analysis of physical properties (Fig. 5b) and siRNA perturbations (Fig. 5c) to reorganize the original data matrix (Fig. 5a) into distinct mechanical phenotypes (Fig. 5d). The result is a  $q \times n$  matrix in which siRNAs (rows) and physical properties (columns) are ordered according to the results from the cross-correlation and unsupervised clustering algorithms. This analysis identified three distinct mechanical phenotypes. The most common phenotype, which we call the Fast/Weak (FW) phenotype, was characterized by an increase in physical properties associated with kinematics and a decrease in physical properties

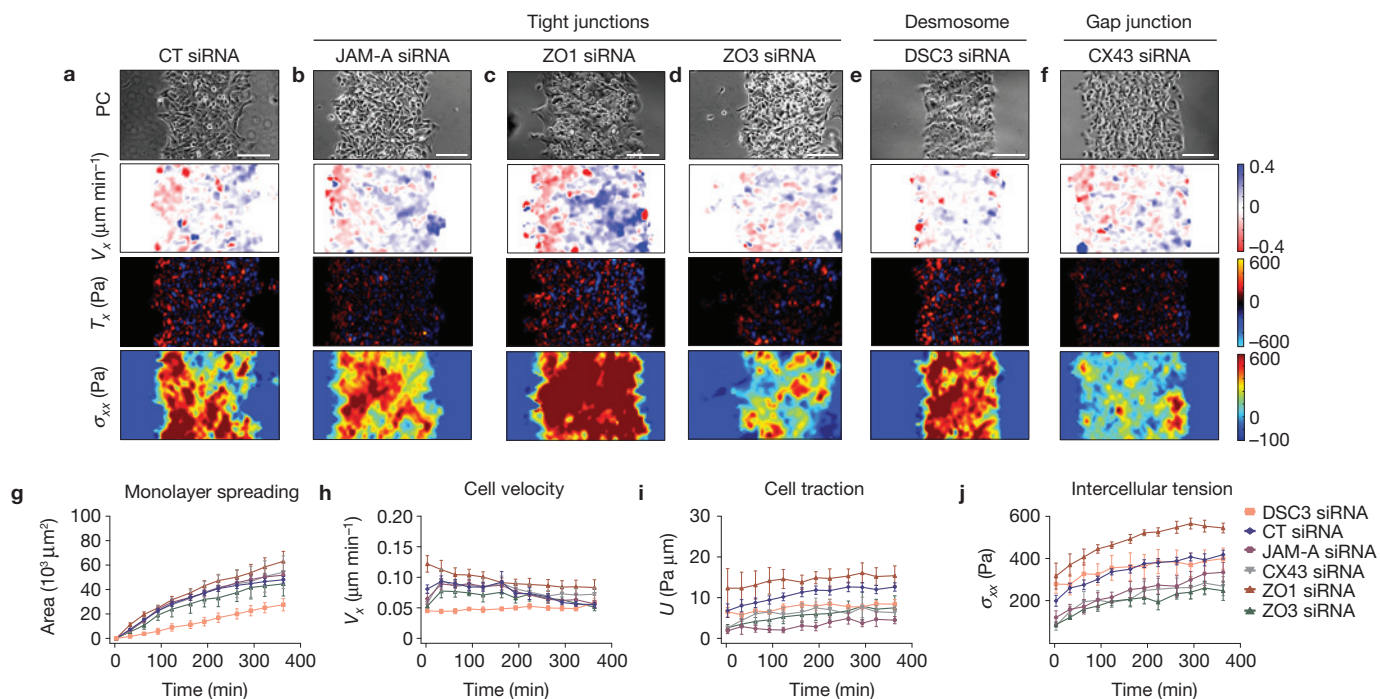


**Figure 4** Downregulation of tight junctions, desmosomes and gap junctions alters monolayer dynamics. (a–f) Representative maps showing the effect of siRNAs on monolayer dynamics after 8 h of expansion. For each siRNA, phase-contrast images (first row), monolayer velocity (second row), traction force (third row), and intercellular tension (fourth row) are shown. Columns show the control case (a) and selected siRNAs targeting tight junctions (b–d), desmosomes (e) and gap junctions (f). Additional time points and siRNA perturbations are shown in Supplementary Figs 5–7. (g–j) Time evolution of monolayer area (shown as the increase from the initial area; g), cell velocity

(h), strain energy density (i), and intercellular tension (j) for the control case and the 5 siRNAs shown in b–f. The time evolution of physical properties in response to all siRNAs is shown in Supplementary Fig. 8. Scale bars, 100  $\mu\text{m}$ . Data are presented as mean  $\pm$  s.e.m.  $n=13$  independent cell monolayers (CT siRNA),  $n=3$  independent cell monolayers (JAM-A siRNA, ZO3 siRNA),  $n=4$  independent cell monolayers (CX43 siRNA),  $n=5$  independent cell monolayers (DSC3 siRNA),  $n=7$  independent cell monolayers (ZO1 siRNA); monolayers were assessed over 10 experiments (CT siRNA), 3 experiments (CX43 siRNA, DSC3 siRNA), 2 experiments (JAM-A siRNA, ZO3 siRNA, ZO1 siRNA).

associated with forces. This phenotype was expressed when proteins from adherens junctions were knocked down. The second phenotype was also characterized by a decrease in physical forces, but in this case kinematics remained largely unchanged. We call this phenotype Steady/Weak (SW). It was observed during loss of function of the gap junction protein CX43, the tight junction proteins CLDN8, ZO-3 and JAM-A, and the desmosomal protein DSC3. The third phenotype was a Fast/Strong (FS) phenotype in which cells migrated and deformed rapidly while exerting strong cell–cell and cell–substrate forces. This phenotype was rare, being observable only in response to siRNA against ZO-1. It is consistent with the recent discoveries that ZO-1 depletion increases contractility of perijunctional actomyosin<sup>42</sup> and that ZO-1 binds integrins in lamellipodia<sup>43</sup>.

### The intercellular adhesome is a highly co-regulated system

Our analysis thus far allowed us to associate specific siRNAs with specific mechanical phenotypes. This association is not necessarily mechanistic at the molecular level, however, because downregulation of one specific protein may lead to changes in physical properties indirectly through the action of other co-regulated proteins. To address co-regulation we selected a subset of siRNA perturbations from our library and measured the effect of these perturbations on the concentrations of cell–cell adhesion proteins. For each siRNA perturbation, we used quantitative western blotting to measure total

protein concentrations relative to control experiments for E-, N-, P-cadherin,  $\beta$ -catenin,  $\alpha$ -catenin, p120, ZO-1 and occludin (see Supplementary Note for a co-regulation analysis of gap junction, tight junction and desmosome hits).

Measurements of protein concentrations showed that each targeted protein was effectively downregulated with an average knockdown efficiency of  $86.3\% \pm 14.5\%$  (mean  $\pm$  s.e.m.; Supplementary Fig. 1c). As expected in a highly co-regulated system<sup>21</sup>, each siRNA altered not only the concentrations of the targeted proteins but also the concentrations of non-targeted proteins. For example, siRNAs against p120 caused a substantial decrease in the concentrations of all cadherins and catenins (Fig. 6a). To study co-regulation patterns systematically we computed the correlation between pairs of proteins by calculating the cosine similarity between the vectors of  $z$ -scores of protein concentrations (columns in Fig. 6a). We then ordered the resulting  $k \times k$  correlation matrix ( $k=8$  proteins) using the unsupervised clustering algorithm (Fig. 6b). All proteins associated with adherens junctions, with the exception of N-cadherin, showed correlations that were highly variable but exclusively positive. These findings show that cadherins and catenins considered in this study are generally not involved in compensatory feedback loops in which a decrease in expression of one protein would be systematically compensated by an increase in expression of another one. Instead, expression levels of different adherens junction proteins in response to siRNA

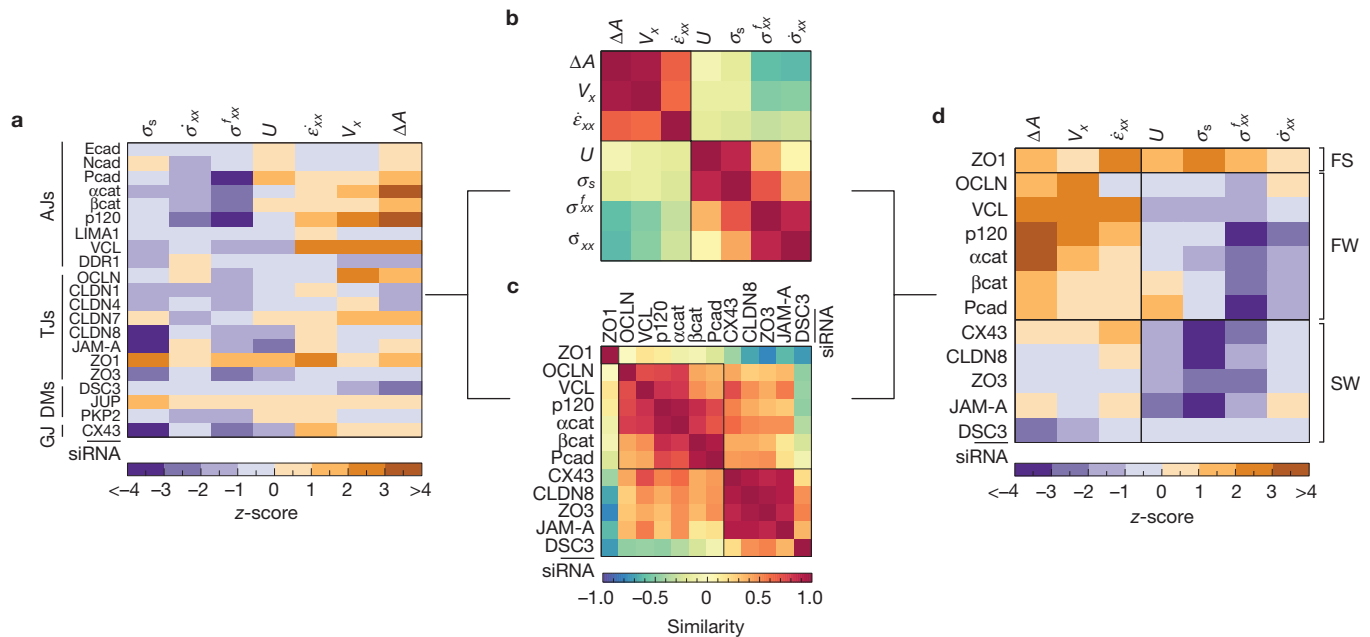


**Figure 5** Cell monolayers with perturbed cell–cell adhesions exhibit distinct mechanical phenotypes. **(a)** Effect of siRNAs on physical properties expressed in terms of their z-scores (see Supplementary Table 1 and Supplementary Note for a description of each physical property). AJs, adherens junctions; TJs, tight junctions; DMs, desmosomes; GJ, gap junctions. **(b)** Correlation between physical properties computed as the cosine similarity between all

possible pairs of columns in **a**. **(c)** Correlation between siRNAs computed as the cosine similarity between all possible pairs of rows in **a**. An unsupervised clustering algorithm was used to order rows and columns in **b**, **c** and to identify clusters whose separation is marked with black lines. **(d)** Reorganization of **a** into phenotypic clusters according to the unsupervised analysis of correlation matrices **b**, **c**. FS (Fast/Strong), FW (Fast/Weak), SW (Steady/Weak).

perturbations varied in parallel. N-cadherin and occludin were the exception to this rule and showed expression patterns that were either uncorrelated or anticorrelated with those of other adherens junction proteins (Fig. 6b).

### P-cadherin predicts the magnitude of intercellular tension, whereas E-cadherin predicts of its build-up rate

We next examined whether protein concentrations might be predictive of the physical properties that characterize epithelial dynamics. As the simplest possible predictive model we considered a linear relationship between any physical property  $X_j$  and any protein concentration  $[p_i]$ :

$$X_j = A + B[p_i] \quad (1)$$

where  $A$  and  $B$  are constant coefficients for each pair protein/physical property (see Supplementary Note for linear models involving multiple protein concentrations).

To assess the predictive power of this model we performed a leave-one-out cross-validation (LOOCV) analysis (Methods). LOOCV analysis revealed that simple linear models involving only one protein were generally poor predictors of physical properties. None of the protein concentrations was able to predict kinematic properties such as monolayer expansion, cellular velocity, or deformation rates. Protein concentrations were also unable to predict the magnitude of traction forces. In contrast, concentrations of E- and P-cadherin were significant predictors of intercellular tension and its time evolution. P-cadherin—but not E-cadherin—was a significant predictor of the average intercellular tension  $\sigma_{xx}^m$  (Fig. 6c and Supplementary Table 2)

as well as of intercellular tension at the end of the experiment  $\sigma_{xx}^f$  (Fig. 6d and Supplementary Table 2). In contrast, E-cadherin—but not P-cadherin—was a significant predictor of the rate at which intercellular tension builds up (Fig. 6e and Supplementary Table 2). Surprisingly, these findings suggest that P-cadherin and E-cadherin play fundamentally distinct roles in controlling force transmission at intercellular junctions. Specifically, they suggest that P-cadherin is involved in the control of equilibrium values of intercellular tension, whereas E-cadherin is involved in the control of the rate at which intercellular tension varies over time.

### P-cadherin and E-cadherin show distinct responses to mechanical stress

Our findings raise the question of how two proteins with high homology play such fundamentally different roles in the regulation of intercellular tension. An appealing possibility is that mechanical tension triggers distinct feedback loops depending on whether it is applied through P-cadherin or E-cadherin. To test this possibility we coated magnetic beads with either P- or E-cadherin and allowed them to bind to cadherin receptors at the apical surface of an MCF10A monolayer. We then used magnetic tweezers to subject the cell–bead junction to a pattern of oscillatory pulling forces<sup>23,44,45</sup> (Fig. 7a). By tracking bead trajectories during force application we studied the mechanical response of the cell to forces exerted through P- or E-cadherin receptors. Pulling on beads coated with E-cadherin led to a pattern of oscillatory bead displacements whose amplitude decreased with time (Fig. 7b,c). This type of cellular response to force has been extensively studied using beads coated with either extracellular

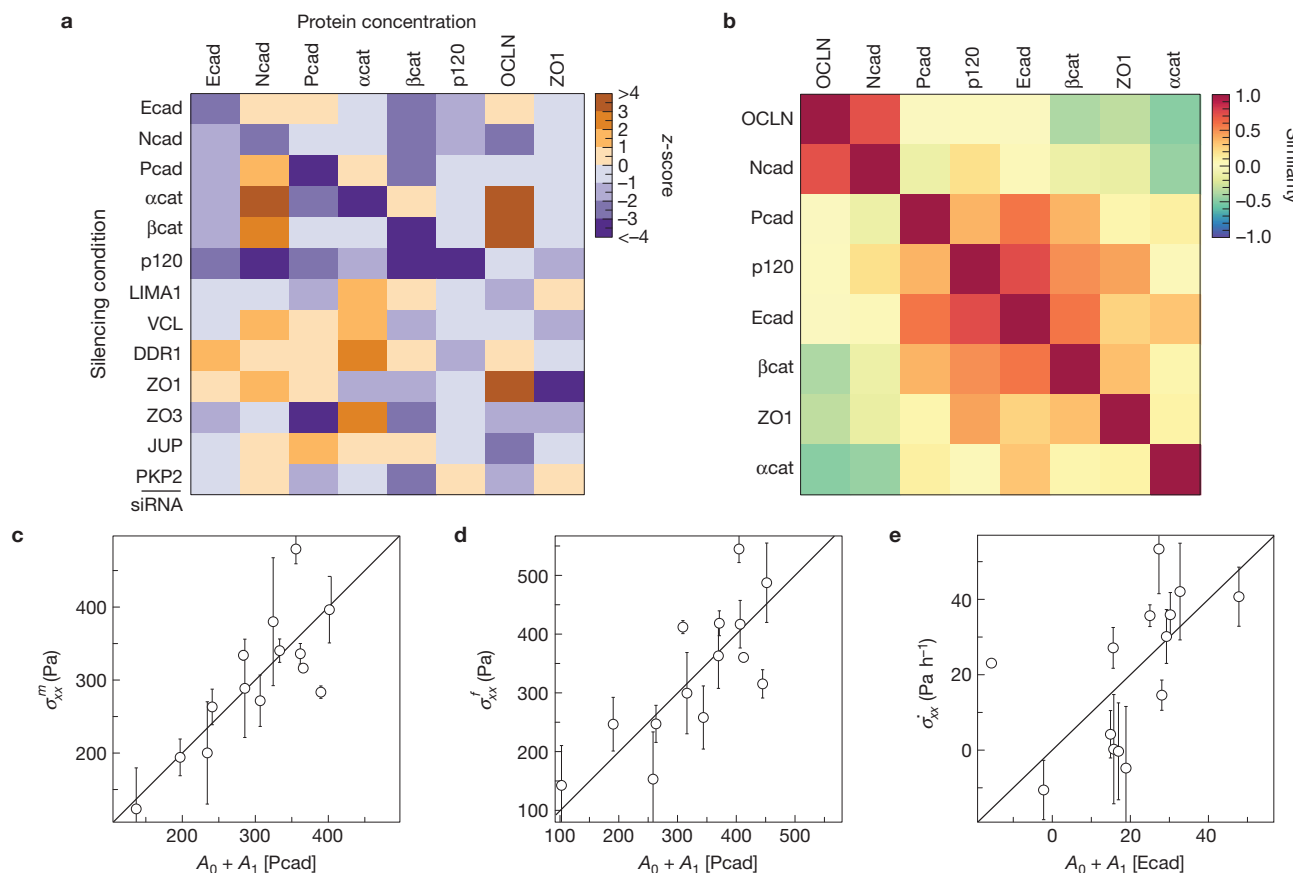


**Figure 6** Protein concentrations predict intercellular forces and their build-up rate. **(a)** z-scores of protein concentrations in response to siRNA perturbations. **(b)** Correlation between protein expression patterns computed as the cosine similarity between columns in **a**. **(c)** The concentration of P-cadherin predicts average intercellular tension. **(d)** The concentration of P-cadherin predicts intercellular tension at the end of the experiment. **(e)** The concentration of E-cadherin predicts the rate of intercellular tension build-up. The x axis in **c–e** shows the values predicted by the one-protein models whereas the y axis shows the experimental values. Each data point corresponds to one siRNA perturbation. Error bars in panels are s.e.m.  $n = 13$  independent cell monolayers

(CT siRNA),  $n = 7$  independent cell monolayers (ZO1 siRNA),  $n = 4$  independent cell monolayers (Pcad siRNA, p120 siRNA, VCL siRNA, JUP siRNA,  $\alpha$ cat siRNA),  $n = 3$  independent cell monolayers (Ecad siRNA, Ncad siRNA,  $\beta$ cat siRNA, LIMA1 siRNA, DDR1 siRNA, ZO3 siRNA, PKP2 siRNA); monolayers were assessed over 10 experiments (CT siRNA), 3 experiments ( $\alpha$ cat siRNA), 2 experiments (Ecad siRNA, Ncad siRNA,  $\beta$ cat siRNA, LIMA1 siRNA, DDR1 siRNA, ZO3 siRNA, PKP2 siRNA, Pcad siRNA, p120 siRNA, VCL siRNA, JUP siRNA, ZO1 siRNA). All predictions in **c–e** were significant to  $P < 0.05$  using a LOOCV. See Supplementary Table 2 for values of prediction errors. See Supplementary Table 3 for predictions by  $N$ -protein models.

matrix proteins<sup>46,47</sup> or cadherins<sup>23,45</sup>; it indicates that tension triggers internal feedback loops that allow the cell to actively adapt to the extracellular force by reinforcing its structural connection with the bead. In contrast, pulling on beads coated with P-cadherin led to a pattern of oscillatory displacements of constant amplitude (Fig. 7b,c), thus indicating that P-cadherin junctions do not reinforce.

Application of pulling forces of varying amplitude revealed a weak tendency of reinforcement through E-cadherin to increase with applied force, and confirmed the absence of reinforcement through P-cadherin (Fig. 7d,e). Decreasing the concentration of P-cadherin at the bead surface changed the initial stiffness of the cell–bead contact but not its time evolution (Fig. 7f–h). In contrast, decreasing the concentration of E-cadherin resulted in no changes in the initial stiffness but in a significant decrease in the stiffening rate (Supplementary Fig. 7f–h). These experiments confirm our predictive models by showing that P-cadherin and E-cadherin play distinct control roles by activating distinct feedback loops downstream of intercellular tension.

### In the absence of E-cadherin, P-cadherin triggers mechanotransduction

In the specific case of E-cadherin depletion, our measurements of mechanotransduction using magnetic tweezers (Fig. 7b,c) and the results of our predictive models (Fig. 6e) would seem to be in contradiction with our measurements of monolayer tension using MSM (Fig. 3b). Indeed, magnetic tweezers experiments and predictive models reveal a key role for E-cadherin in the dynamic regulation of monolayer tension (Figs 7 and 6e), whereas knocking down E-cadherin did not alter monolayer tension and cohesion (Figs 3b and 7i,j). This apparent contradiction could originate from a functional redundancy between E-cadherin and P-cadherin. To explore this possibility we used magnetic tweezers to pull on beads coated with P-cadherin attached to cells depleted of E-cadherin. Under such conditions, and contrary to the case of control cells, pulling on P-cadherin caused reinforcement of the cell–bead contact (Fig. 7b,c). Thus P-cadherin is able to trigger mechanotransduction feedback loops, but it does so only in the absence of



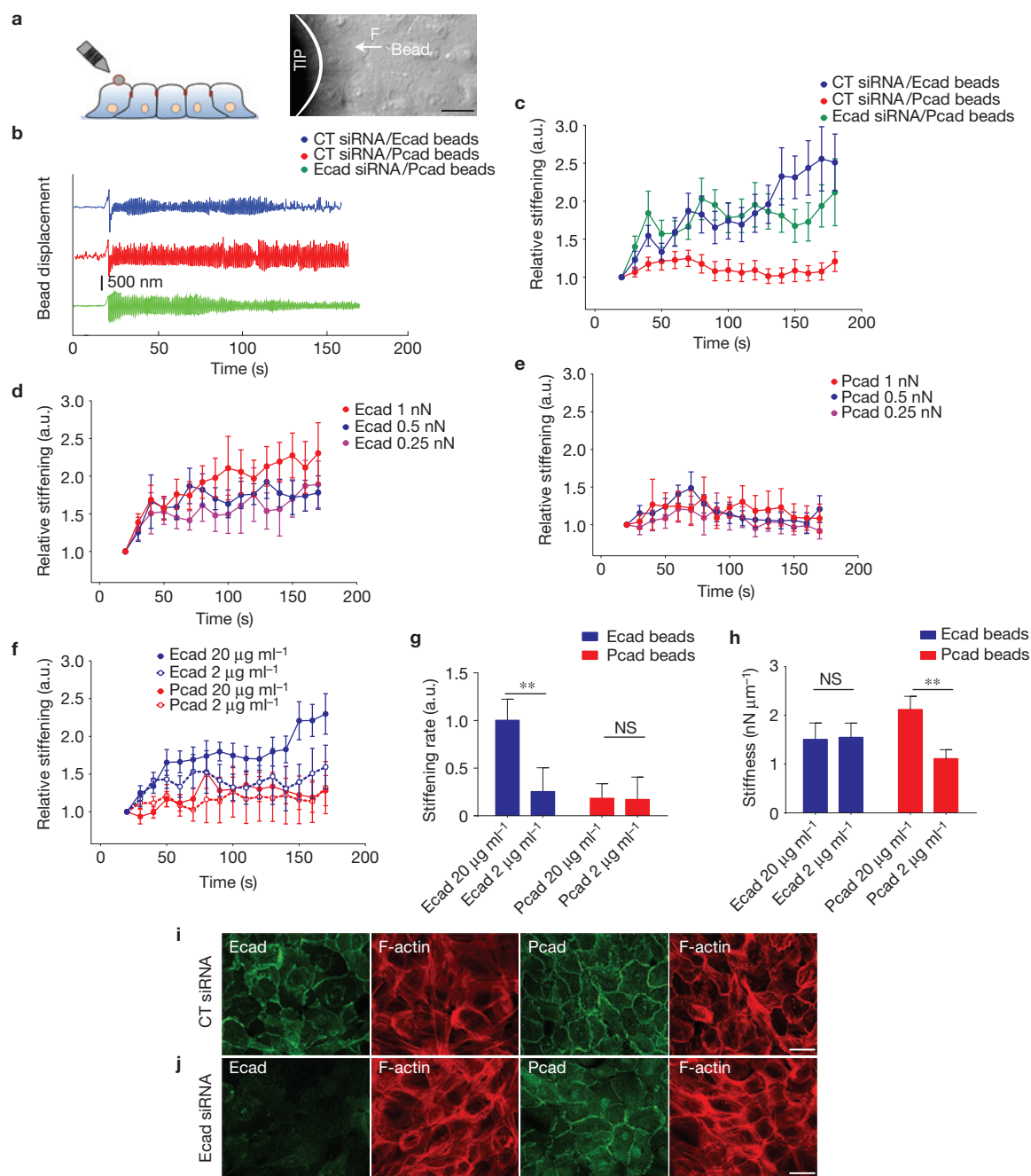


**Figure 7** Force applied to E-cadherin triggers reinforcement feedback loops whereas force applied to P-cadherin does not. (a) Experimental set-up. Magnetic beads coated with E-cadherin or P-cadherin were attached to the apical surface of MCF10A monolayers and subjected to a series of force pulses using magnetic tweezers. (b) Representative examples of bead displacements for P-cadherin-coated beads bound to control cells (red), E-cadherin-coated beads bound to control cells (blue), and P-cadherin-coated beads bound to Ecad siRNA cells (green). (c) Relative stiffening of the cell-bead contact for P-cadherin-coated beads bound to control cells (red,  $n=22$  beads pooled from 9 independent wells), E-cadherin-coated beads bound to control cells (blue,  $n=26$  beads pooled from 9 independent wells), and P-cadherin-coated beads bound to cells depleted of E-cadherin (green,  $n=23$  beads pooled from 9 independent wells). (d) Relative stiffening of the junction between cells and beads coated with E-cadherin in response to oscillatory forces of amplitude 0.25 nN (purple,  $n=22$  beads pooled from 9 independent wells), 0.5 nN (blue,  $n=20$  beads pooled from 9 independent wells) and 1 nN (red,  $n=13$  beads pooled

from 9 independent wells). (e) Relative stiffening of the junction between cells and beads coated with P-cadherin in response to oscillatory forces of amplitude 0.25 nN (purple,  $n=16$  beads pooled from 9 independent wells), 0.5 nN (blue,  $n=16$  beads pooled from 9 independent wells) and 1 nN (red,  $n=15$  beads pooled from 9 independent wells). (f) Relative stiffening of the junction between cells and beads coated with E-cadherin (blue) and P-cadherin (red) using coating solutions of  $2 \mu\text{g ml}^{-1}$  (open symbols) or  $20 \mu\text{g ml}^{-1}$  (filled symbols). (g) Stiffening rate (slope of curves in f) of the cell-bead contact. (h) Initial stiffness of the cell-bead contact. In c-h data are represented as mean + s.e.m. \*\* indicates  $P < 0.01$  (Mann-Whitney Rank Sum  $t$ -test). NS indicates nonsignificant comparisons. In f-h  $n=17$  beads pooled from 6 independent wells for Ecad  $20 \mu\text{g ml}^{-1}$ ;  $n=16$  beads pooled from 6 independent wells for Ecad  $2 \mu\text{g ml}^{-1}$ ;  $n=16$  beads pooled from 6 independent wells for Pcad  $20 \mu\text{g ml}^{-1}$ ;  $n=17$  beads pooled from 6 independent wells for Pcad  $2 \mu\text{g ml}^{-1}$ . (i, j) Staining of E-cadherin, P-cadherin and F-actin (phalloidin) under control conditions (i) and after E-cadherin knock down (j). Scale bars,  $20 \mu\text{m}$  (a, i, j).

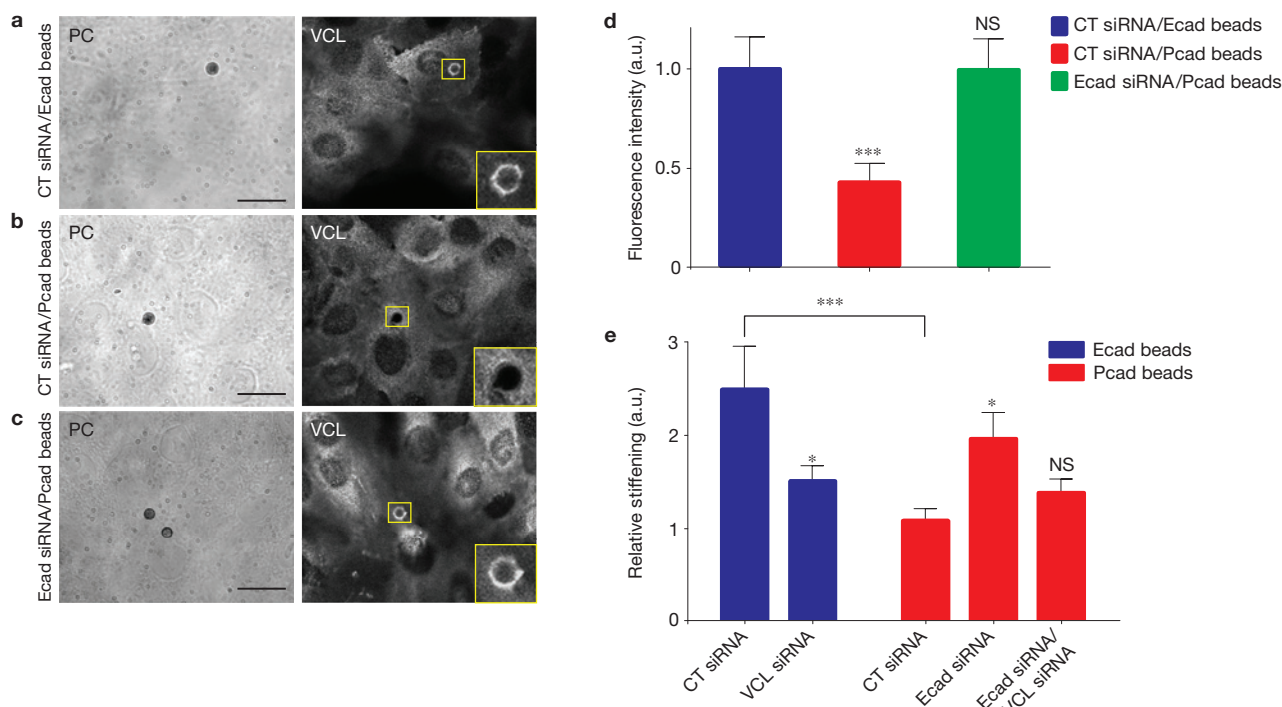


**Figure 8** Vinculin is involved in mechanotransduction through P-cadherin and E-cadherin. (a) Phase-contrast (PC) image (left) and staining (right) of vinculin (VCL) after force application at the contact between control cells and beads coated with E-cadherin. (b) Phase-contrast image (left) and staining (right) of vinculin after force application at the contact between control cells and beads coated with P-cadherin. (c) Phase-contrast image (left) and staining (right) of vinculin (VCL) after force application at the contact between cells depleted of E-cadherin and beads coated with P-cadherin. (d) Vinculin recruitment at the cell–bead contact for E-cadherin-coated beads bound to control cells (blue,  $n=25$  beads pooled from 12 independent wells), P-cadherin-coated beads bound to control cells (red,  $n=28$  beads pooled from 12 independent wells) and P-cadherin-coated beads bound to cells depleted of E-cadherin (green,  $n=20$  beads

pooled from 9 independent wells). Data are presented as mean  $\pm$  s.e.m. (normalized to VCL recruitment in E-cadherin-coated beads bound to control cells). (e) Relative stiffening at the end of bead pulling assays (180 s). Beads were coated with P-cadherin (blue) or E-cadherin (red). In e,  $n=26$  beads pooled from 9 independent wells for CT siRNA/Ecad beads;  $n=22$  beads pooled from 9 independent wells for VCL siRNA/Ecad beads;  $n=22$  beads pooled from 9 independent wells for CT siRNA/Pcad beads;  $n=23$  beads pooled from 9 independent wells for Ecad siRNA/Pcad beads;  $n=36$  beads pooled from 9 independent wells for Ecad siRNA/VCL siRNA/Pcad beads. Data are represented as mean  $\pm$  s.e.m. \* indicates  $P < 0.05$ , \*\*\* indicates  $P < 0.001$  when compared with CT siRNA. NS indicates nonsignificant comparisons (Mann–Whitney rank sum  $t$ -test). Scale bars,  $10 \mu\text{m}$  (a–c).

E-cadherin. Such functional redundancy reconciles the apparent conflict between our distinct measurement techniques and analysis strategies; when E-cadherin is knocked down, P-cadherin is able to take over its role as a tension regulator, thereby preventing a decrease in intercellular tension.

### Vinculin is involved in mechanotransduction through P-cadherin and E-cadherin

Our previous experiments raise the possibility that mechanotransduction through P- and E-cadherin is mediated by the same molecular pathway but that E-cadherin has a higher affinity than P-cadherin for that pathway. An appealing molecular candidate to be involved in this common pathway is vinculin, which binds to a cryptic site of  $\alpha$ -catenin to trigger mechanotransduction<sup>48,49</sup>. To test this possibility we first measured the localization of vinculin after force application. After pulling on E-cadherin in control cells we observed an accumulation of vinculin at the cell–bead contact (Fig. 8a,d), in agreement with previous findings<sup>45,50</sup>. This accumulation was significantly higher than that observed after pulling on P-cadherin in control cells (Fig. 8b,d). However, after pulling on P-cadherin in cells depleted of E-cadherin,

the levels of vinculin accumulation at the cell–bead contact were similar to those observed in beads coated with E-cadherin in control cells (Fig. 8c,d). These experiments show that vinculin accumulation at the cell–bead contacts parallels mechanotransduction responses.

To further support the involvement of vinculin in mechanotransduction through both E- and P-cadherin we reasoned that vinculin knockdown should impair E-cadherin and P-cadherin reinforcement. Consistent with this hypothesis, pulling on magnetic beads coated with E-cadherin in cells depleted of vinculin resulted in weaker reinforcement (Fig. 8e). Similarly, pulling on magnetic beads coated with P-cadherin in cells depleted of both E-cadherin and vinculin also led to weaker reinforcement (Fig. 8e). Together, these experiments support that P- and E-cadherin compete for a common mechanotransduction pathway involving vinculin.

### DISCUSSION

Epithelial dynamics is traditionally interpreted in the context of a smooth or abrupt transition between epithelial and mesenchymal states; as the concentrations of intercellular adhesion proteins decrease, cells within tissues lose cohesiveness and speed up

migration<sup>51,52</sup>. Here we showed that the phenotypic plasticity of monolayer dynamics is much richer than previously thought; by expressing distinct combinations of cell–cell adhesion proteins, cells control their velocity and intercellular tension independently.

Recently, experiments using nearly identical approaches have led to conflicting conclusions as regards the correlation between intercellular force and the localization of E-cadherin at cell–cell junctions<sup>37–39</sup>. Our findings suggest that this discrepancy might be explained by different confounding factors. First, E-cadherin should not be regarded as the only cadherin involved in the regulation of intercellular tension; other cadherins, such as P-cadherin, should be taken into account to understand force balance at intercellular junctions. Second, different cadherins can exhibit mechanical redundancy when expressed in isolation but trigger different mechanotransduction feedback loops when expressed in conjunction. Finally, the total protein concentration, and not necessarily the amount of protein that localizes at intercellular junctions, is a robust determinant of intercellular tension. Once these considerations are taken into account, our study shows that simple models can predict monolayer tension and its build-up rate. Given the high connectivity of cell–cell adhesion proteins (E-cadherin has 96 known binding partners and  $\beta$ -catenin has 243 (ref. 53)), the existence of such simple models is remarkable.

When E-cadherin was knocked down, the rate of stress build-up of the cell monolayer remained unaltered. This result was not well captured by our predictive model based solely on E-cadherin concentration (see leftmost data point in Fig. 6e). Using magnetocytometry, we showed that this discrepancy originates from a functional redundancy between P- and E-cadherin (Fig. 7). Interestingly, this redundancy seemed to be active only at relatively low concentrations of E-cadherin, suggesting that E-cadherin has a much higher affinity than P-cadherin for the mechanotransduction machinery of the cell. In this connection, it is worth emphasizing that models involving concentrations of multiple proteins produced much more accurate predictions than one-protein models.

P- and E-cadherin have highly homologous sequences but are attributed markedly different roles in physiology and cancer. They are usually co-expressed in the basal layer of stratified epithelia, where proliferation, differentiation and compartmentalization take place<sup>54,55</sup>. In contrast only E-cadherin is usually expressed in suprabasal differentiated layers where mechanical function is less diverse. In cancer, E-cadherin expression is generally associated with positive prognosis, whereas P-cadherin expression is associated with increased cancer cell migration and invasion<sup>54,55</sup>. Interestingly, in cancers where only P- or E-cadherin are expressed, both proteins act as suppressors of cancer invasion<sup>56–59</sup>. Such behaviour is consistent with our findings that P-cadherin and E-cadherin play a similar mechanical role when one of them is expressed dominantly. In contrast, aggressive invasion is observed when P- and E-cadherin are jointly expressed<sup>22</sup>. Further studies should address whether underlying mechanisms involve the competition of cadherins for a joint mechanotransduction pathway as reported in our study.

The simultaneous expression of two distinct proteins, one proportional to the magnitude of a physical quantity and one proportional to the time derivative of this quantity, provides the cell with advanced control capabilities. In proportional control systems, which are the simplest control systems involving feedback loops, the

control signal is proportional to the difference between the value of the output and its desired setpoint<sup>60</sup>. Control theory shows that the efficiency of this control strategy is significantly improved if the control signal also takes into account the time derivative of the output, or in other words, how fast the desired setpoint is being reached<sup>60,61</sup>. Derivative control action of this kind is widely used in engineering to compensate rapid changes in the output and to reduce instabilities. Here we showed that the concentrations of P- and E-cadherin are good predictors of intercellular tension and its time derivative, respectively. These findings raise the possibility that adherens junctions act as proportional-derivative feedback systems to control intercellular tension. □

## METHODS

Methods and any associated references are available in the [online version of the paper](#).

*Note: Supplementary Information is available in the online version of the paper*

## ACKNOWLEDGEMENTS

We thank F. Supek, B. Lehner, A. Brugués and R. Vincent for discussions, R. Zaidel-Bar for sharing unpublished data, and E. Sahai for contributing reagents. This research was supported by the European Research Council (StG-242993 and CoG-616480 to X.T.), the 7th European Community Framework Programme (PCIG10-GA-2011-303848 to P.R.-C., PIRG-GA-2010-277166 to R.G., PIRG-GA-2010-268342 to M.S.-P., FET Grant 317532 to M.S.-P. and R.G.), the Spanish Ministerio de Economía y Competitividad (BFU2012-38146 to X.T., DPI2013-43727-R to J.J.M., FIS2010-18639 and FIS2013-47532-C3 to M.S.-P. and R.G., BFU2011-23111 to P.R.-C., Juan de la Cierva Fellowship JCI-2012-15123 to V.C.), the National Institutes of Health (R01HL107561 to X.T.), Fundació La Caixa, Fundació la Marató de TV3 (20133330 to P.R.-C.), and the James S. McDonnell Foundation (R.G. and M.S.-P.).

## AUTHOR CONTRIBUTIONS

E.B. and X.T. conceived the study and designed experiments. E.B., M.B.-M. and A.E.-A. performed experiments. E.B., V.C. and A.E.-A. analysed data. X.S.-P. and P.R.-C. developed data analysis tools. V.C. and J.J.M. developed computational mechanics tools. M.S.-P. and R.G. performed unsupervised clustering analysis and LOOCV analysis. E.B., M.S.-P., R.G. and X.T. wrote the manuscript. All authors discussed and interpreted results and commented on the manuscript.

## COMPETING FINANCIAL INTERESTS

The authors declare no competing financial interests.

Published online at [www.nature.com/doi/10.1038/ncb3135](http://www.nature.com/doi/10.1038/ncb3135)

Reprints and permissions information is available online at [www.nature.com/reprints](http://www.nature.com/reprints)

- Friedl, P. & Gilmour, D. Collective cell migration in morphogenesis, regeneration and cancer. *Nat. Rev. Mol. Cell Biol.* **10**, 445–457 (2009).
- Weber, G. F., Bjerke, M. A. & DeSimone, D. W. A mechanoresponsive cadherin-keratin complex directs polarized protrusive behavior and collective cell migration. *Dev. Cell* **22**, 104–115 (2012).
- Heisenberg, C. P. & Bellaiche, Y. Forces in tissue morphogenesis and patterning. *Cell* **153**, 948–962 (2013).
- Leckband, D. E., le Duc, Q., Wang, N. & de Rooij, J. Mechanotransduction at cadherin-mediated adhesions. *Curr. Opin. Cell Biol.* **23**, 523–530 (2011).
- Budnar, S. & Yap, A. S. A mechanobiological perspective on cadherins and the actin-myosin cytoskeleton. *F1000Prime Rep.* **5**, 35 (2013).
- Tambe, D. T. *et al.* Collective cell guidance by cooperative intercellular forces. *Nat. Mater.* **10**, 469–475 (2011).
- Theveneau, E. *et al.* Chase-and-run between adjacent cell populations promotes directional collective migration. *Nat. Cell Biol.* **15**, 763–772 (2013).
- Campinho, P. *et al.* Tension-oriented cell divisions limit anisotropic tissue tension in epithelial spreading during zebrafish epiboly. *Nat. Cell Biol.* **15**, 1405–1414 (2013).
- Bosveld, F. *et al.* Mechanical control of morphogenesis by Fat/Dachsous/Four-jointed planar cell polarity pathway. *Science* **336**, 724–727 (2012).
- Legoff, L., Rouault, H. & Lecuit, T. A global pattern of mechanical stress polarizes cell divisions and cell shape in the growing *Drosophila* wing disc. *Dev. Suppl.* **140**, 4051–4059 (2013).
- Brugués, A. *et al.* Forces driving epithelial wound healing. *Nat. Phys.* **10**, 683–690 (2014).
- Rauzi, M., Lenne, P. F. & Lecuit, T. Planar polarized actomyosin contractile flows control epithelial junction remodelling. *Nature* **468**, 1110–1114 (2010).

13. Serra-Picamal, X. *et al.* Mechanical waves during tissue expansion. *Nat. Phys.* **8**, 628–634 (2012).
14. Foty, R. A. & Steinberg, M. S. The differential adhesion hypothesis: a direct evaluation. *Dev. Biol.* **278**, 255–263 (2005).
15. Borghi, N. *et al.* E-cadherin is under constitutive actomyosin-generated tension that is increased at cell–cell contacts upon externally applied stretch. *Proc. Natl Acad. Sci. USA* **109**, 12568–12573 (2012).
16. Maitre, J. L. & Heisenberg, C. P. Three functions of cadherins in cell adhesion. *Curr. Biol.* **23**, R626–R633 (2013).
17. Zaidel-Bar, R. Cadherin adhesome at a glance. *J. Cell Sci.* **126**, 373–378 (2013).
18. Nieman, M. T., Prudoff, R. S., Johnson, K. R. & Wheelock, M. J. N-cadherin promotes motility in human breast cancer cells regardless of their E-cadherin expression. *J. Cell Biol.* **147**, 631–644 (1999).
19. Ribeiro, A. S. *et al.* Extracellular cleavage and shedding of P-cadherin: a mechanism underlying the invasive behaviour of breast cancer cells. *Oncogene* **29**, 392–402 (2010).
20. Battle, E. *et al.* The transcription factor snail is a repressor of E-cadherin gene expression in epithelial tumour cells. *Nat. Cell Biol.* **2**, 84–89 (2000).
21. Kumper, S. & Ridley, A. J. p120ctn and P-cadherin but not E-cadherin regulate cell motility and invasion of DU145 prostate cancer cells. *PLoS ONE* **5**, e11801 (2010).
22. Ribeiro, A. S. *et al.* P-cadherin functional role is dependent on E-cadherin cellular context: a proof of concept using the breast cancer model. *J. Pathol.* **229**, 705–718 (2013).
23. Tabdili, H. *et al.* Cadherin-dependent mechanotransduction depends on ligand identity but not affinity. *J. Cell Sci.* **125**, 4362–4371 (2012).
24. Buckley, C. D. *et al.* Cell adhesion. The minimal cadherin-catenin complex binds to actin filaments under force. *Science* **346**, 1254211 (2014).
25. Abe, K. & Takeichi, M. EPLIN mediates linkage of the cadherin catenin complex to F-actin and stabilizes the circumferential actin belt. *Proc. Natl Acad. Sci. USA* **105**, 13–19 (2008).
26. Yamada, S., Pokutta, S., Drees, F., Weis, W. I. & Nelson, W. J. Deconstructing the cadherin-catenin-actin complex. *Cell* **123**, 889–901 (2005).
27. Runkle, E. A. & Mu, D. Tight junction proteins: from barrier to tumorigenesis. *Cancer Lett.* **337**, 41–48 (2013).
28. Harris, A. R. *et al.* Characterizing the mechanics of cultured cell monolayers. *Proc. Natl Acad. Sci. USA* **109**, 16449–16454 (2012).
29. Herrmann, H., Bar, H., Kreplak, L., Strelkov, S. V. & Aebi, U. Intermediate filaments: from cell architecture to nanomechanics. *Nat. Rev. Mol. Cell Biol.* **8**, 562–573 (2007).
30. Wang, N. & Stamenovic, D. Contribution of intermediate filaments to cell stiffness, stiffening, and growth. *Am. J. Physiol.* **279**, C188–C194 (2000).
31. Bao, L., Sachs, F. & Dahl, G. Connexins are mechanosensitive. *Am. J. Physiol.* **287**, C1389–C1395 (2004).
32. Poujade, M. *et al.* Collective migration of an epithelial monolayer in response to a model wound. *Proc. Natl Acad. Sci. USA* **104**, 15988–15993 (2007).
33. Hur, S. S. *et al.* Roles of cell confluency and fluid shear in 3-dimensional intracellular forces in endothelial cells. *Proc. Natl Acad. Sci. USA* **109**, 11110–11115 (2012).
34. Tambe, D. T. *et al.* Monolayer stress microscopy: limitations, artifacts, and accuracy of recovered intercellular stresses. *PLoS ONE* **8**, e55172 (2013).
35. Trepat, X. & Fredberg, J. J. Plithotaxis and emergent dynamics in collective cellular migration. *Trends Cell Biol.* **21**, 638–646 (2012).
36. Trepat, X. *et al.* Physical forces during collective cell migration. *Nat. Phys.* **5**, 426–430 (2009).
37. Liu, Z. *et al.* Mechanical tugging force regulates the size of cell–cell junctions. *Proc. Natl Acad. Sci. USA* **107**, 9944–9949 (2010).
38. Maruthamuthu, V., Sabass, B., Schwarz, U. S. & Gardel, M. L. Cell–ECM traction force modulates endogenous tension at cell–cell contacts. *Proc. Natl Acad. Sci. USA* **108**, 4708–4713 (2011).
39. Ng, M. R., Besser, A., Brugge, J. S. & Danuser, G. Mapping the dynamics of force transduction at cell–cell junctions of epithelial clusters. *eLife* **4**, e03282 (2014).
40. Simpson, K. J. *et al.* Identification of genes that regulate epithelial cell migration using an siRNA screening approach. *Nat. Cell Biol.* **10**, 1027–1038 (2008).
41. Sales-Pardo, M., Guimera, R., Moreira, A. A. & Amaral, L. A. Extracting the hierarchical organization of complex systems. *Proc. Natl Acad. Sci. USA* **104**, 15224–15229 (2007).
42. Fanning, A. S., Van Itallie, C. M. & Anderson, J. M. Zonula occludens-1 and -2 regulate apical cell structure and the zonula adherens cytoskeleton in polarized epithelia. *Mol. Biol. Cell* **23**, 577–590 (2012).
43. Tuomi, S. *et al.* PKCepsilon regulation of an  $\alpha 5$  integrin-ZO-1 complex controls lamellae formation in migrating cancer cells. *Sci. Signal.* **2**, ra32 (2009).
44. Bausch, A. R., Moller, W. & Sackmann, E. Measurement of local viscoelasticity and forces in living cells by magnetic tweezers. *Biophys. J.* **76**, 573–579 (1999).
45. Le Duc, Q. *et al.* Vinculin potentiates E-cadherin mechanosensing and is recruited to actin-anchored sites within adherens junctions in a myosin II-dependent manner. *J. Cell Biol.* **189**, 1107–1115 (2010).
46. Riveline, D. *et al.* Focal contacts as mechanosensors: externally applied local mechanical force induces growth of focal contacts by an mDia1-dependent and ROCK-independent mechanism. *J. Cell Biol.* **153**, 1175–1186 (2001).
47. Roca-Cusachs, P., Gauthier, N. C., Del Rio, A. & Sheetz, M. P. Clustering of  $\alpha 5 \beta 1$  integrins determines adhesion strength whereas  $\alpha (v) \beta 3$  and talin enable mechanotransduction. *Proc. Natl Acad. Sci. USA* **106**, 16245–16250 (2009).
48. Yonemura, S., Wada, Y., Watanabe, T., Nagafuchi, A. & Shibata, M.  $\alpha$ -Catenin as a tension transducer that induces adherens junction development. *Nat. Cell Biol.* **12**, 533–542 (2010).
49. Yao, M. *et al.* Force-dependent conformational switch of  $\alpha$ -catenin controls vinculin binding. *Nat. Commun.* **5**, 4525 (2014).
50. Barry, A. K. *et al.*  $\alpha$ -catenin cytomechanics—role in cadherin-dependent adhesion and mechanotransduction. *J. Cell Sci.* **127**, 1779–1791 (2014).
51. Cano, A. *et al.* The transcription factor snail controls epithelial–mesenchymal transitions by repressing E-cadherin expression. *Nat. Cell Biol.* **2**, 76–83 (2000).
52. Thiery, J. P., Acloque, H., Huang, R. Y. & Nieto, M. A. Epithelial–mesenchymal transitions in development and disease. *Cell* **139**, 871–890 (2009).
53. Stark, C. *et al.* BioGRID: a general repository for interaction datasets. *Nucleic Acids Res.* **34**, D535–D539 (2006).
54. Albergaria, A. *et al.* P-cadherin role in normal breast development and cancer. *Int. J. Dev. Biol.* **55**, 811–822 (2011).
55. Van Roy, F. Beyond E-cadherin: roles of other cadherin superfamily members in cancer. *Nat. Rev. Cancer* **14**, 121–134 (2014).
56. Vlemminckx, K., Vakaet, L. Jr, Mareel, M., Fiers, W. & van Roy, F. Genetic manipulation of E-cadherin expression by epithelial tumor cells reveals an invasion suppressor role. *Cell* **66**, 107–119 (1991).
57. Wong, A. S. & Gumbiner, B. M. Adhesion-independent mechanism for suppression of tumor cell invasion by E-cadherin. *J. Cell Biol.* **161**, 1191–1203 (2003).
58. Van Marck, V. *et al.* P-cadherin promotes cell–cell adhesion and counteracts invasion in human melanoma. *Cancer Res.* **65**, 8774–8783 (2005).
59. Jacobs, K. *et al.* P-cadherin counteracts myosin II-B function: implications in melanoma progression. *Mol. Cancer* **9**, 255 (2010).
60. Bechhoefer, J. Feedback for physicists: a tutorial essay on control. *Rev. Mod. Phys.* **77**, 783–836 (2005).
61. Cloutier, M. & Wellstead, P. The control systems structures of energy metabolism. *J. R. Soc. Interface* **7**, 651–665 (2010).

## METHODS

**MCF10A cell culture.** MCF10A cells were grown on DMEM-F12 media supplemented with 5% horse serum, 100 U ml<sup>-1</sup> penicillin, 100 µg ml<sup>-1</sup> streptomycin, 20 ng ml<sup>-1</sup> EGF, 0.5 mg ml<sup>-1</sup> hydrocortisone, 100 ng ml<sup>-1</sup> cholera toxin and 10 µg ml<sup>-1</sup> insulin.

**Polyacrylamide gel substrates.** Polyacrylamide gels with a Young's modulus of 12 kPa were prepared as described previously<sup>13,32,63</sup>. Briefly, a solution containing 19% acrylamide, 8% bis-acrylamide, 0.5% ammonium persulphate, 0.05% tetramethylethylenediamine, 0.64% of 200-nm-diameter red fluorescent carboxylate-modified beads and 2 mg ml<sup>-1</sup> NH-acrylate was prepared and allowed to polymerize. After polymerization, gels were incubated with 0.1 mg ml<sup>-1</sup> of collagen I overnight.

**PDMS membranes.** Polydimethylsiloxane (PDMS) membranes were fabricated according to procedures described previously<sup>13,32,64</sup>. Briefly, SU8-50 masters containing rectangles of 300 × 2,500 µm were raised using conventional photolithography. Uncured PDMS was spin-coated on the masters to a thickness lower than the height of the SU8 feature (35 µm) and cured for 2 h at 60 °C. A thick border of PDMS was left at the edges of the membranes for handling purposes. PDMS was then peeled off from the master and kept in ethanol at 4 °C until use.

**Monolayer patterning.** To pattern the cells on top of the polyacrylamide gels, a PDMS membrane was deposited on top of the polyacrylamide gel and 20,000 cells were seeded within the rectangle defined by the PDMS stencil. Cells were allowed to adhere and proliferate on the gel for 5 h. Forty minutes before time-lapse analysis, the PDMS membrane was carefully removed allowing the cells to migrate towards the freely available substrate.

**siRNA transfection.** siRNA reverse transfections were performed by mixing Lipofectamine RNAiMAX Reagent with 100 picomoles of a pool of 3 siRNAs and 450,000 freshly trypsinized MCF10A cells (see Supplementary Table 4 for siRNA sequences). Cells were then seeded on 6-well plates. Five days after transfection, cells were trypsinized and seeded on soft polyacrylamide gels. Approximately 90% of the cells were successfully transfected as measured using Block-it Alexa Fluor Red Fluorescent Oligo.

**Real-time PCR.** Real-time PCR experiments were performed according to the manufacturer's instructions (Applied Biosystems). Total mRNA was extracted from MCF10A control and knockdown cells using the PARIS kit. RNA samples were reverse-transcribed into cDNA using the High Capacity RNA-to-cDNA master mix. Taqman Gene Expression Assays were used to detect endogenous mRNA levels. The housekeeping gene *RPS18* was used as an endogenous control for normalization (see Supplementary Table 4 for Taqman probe list). PCR was performed on a 7500 Fast Real Time PCR System (Applied Biosystems).

**Protein quantification.** Protein expression levels were measured using western blotting. Cells were lysed for protein extraction using lysis buffer (Tris 20 mM pH 8, NaCl 150 mM, EDTA 1 mM, EGTA 1 mM, 1% Triton X-100, antipain 1 µg ml<sup>-1</sup>, pepstatin 1 µg ml<sup>-1</sup>, benzamidin 15 µg ml<sup>-1</sup>, leupeptin 1 µg ml<sup>-1</sup>, orthovanadate 0.1 mM). Cell lysates were then mixed with Laemmli 1× and heated at 95 °C for 5 min. Next, cell lysates were loaded to 4–20% polyacrylamide gels (Bio-Rad) for electrophoresis. Proteins were then transferred to a nitrocellulose membrane (Whatman, GE Healthcare Life Sciences), which was blocked with 5% dry milk-Tris buffer saline–0.2% Tween, and incubated with primary antibodies (overnight at 4 °C) followed by the horseradish-peroxidase-coupled secondary antibodies (1 h, room temperature). Bands were revealed using the LumiLight kit (Roche) and the intensity of the bands was quantified using ImageJ software. Tubulin was used as an endogenous control for normalization. Protein concentrations are reported relative to the control.

**Immunostaining.** MCF10A cells were washed with PBS, fixed with 3% paraformaldehyde for 10 min and permeabilized in 0.1% Triton X-100 for 5 min. Cells were blocked in 10% FBS for 1 h before being incubated for 4 h with primary antibodies. After incubation with the appropriate fluorescence-conjugated secondary antibodies, cells were washed and mounted in Mowiol reagent. Images were acquired with a Nikon C1Si confocal microscope, using a ×60 1.4NA lens.

**Antibodies.** The primary antibodies used were: anti-E-cadherin monoclonal antibody (clone 36, BD Transduction Laboratories, no. 610181), anti-N-cadherin monoclonal antibody (clone 8C11, Thermo Scientific, no. MA1-2002), anti-P-cadherin monoclonal antibody (clone 6A9, Upstate MerckMillipore, no. 05-916), anti-β-catenin monoclonal antibody (clone 14, BD Transduction Laboratories, no. 610153), anti-α-catenin monoclonal antibody (clone 15D9, Enzo Life Sciences,

no. ALX-804-101-C100), anti-p120 catenin monoclonal antibody (clone 98, BD Transduction Laboratories, no. 610133), anti-occludin monoclonal antibody (clone OC-3F10, Invitrogen, no. 33-1500), anti-ZO1 rabbit polyclonal antibody (Invitrogen, no. 61-7300), anti-α-tubulin monoclonal antibody (clone B-5-1-2, Sigma-Aldrich, no. T5168), anti-vinculin monoclonal antibody (clone 7F9, EMD Millipore, no. MAB6574), anti-desmocolin3 rabbit polyclonal antibody (ABGENT, no. AP16771b), anti-JAM-A monoclonal antibody (clone EP1042Y, EMD Millipore, no. 04-593), anti-connexin43 rabbit polyclonal antibody (EMD Millipore, no. AB1728), anti-ZO3 monoclonal antibody (clone D57G7, Cell Signaling, no. 3704). For western blotting, all of the antibodies were diluted 1:500, except anti-α-tubulin 1:10,000. For immunofluorescence, all of the antibodies were diluted 1:200. The secondary antibodies used for western blots were: peroxidase-conjugated anti-mouse IgG (Jackson Immuno Research, no. 715-035-151) and peroxidase-conjugated anti-rabbit IgG (Merck Millipore, no. AP132P) and were diluted 1:5,000. The secondary antibodies used for immunofluorescence were: Alexa Fluor 488 anti-rabbit (Invitrogen, Molecular Probes, no. A-21206) and Alexa Fluor 488 anti-mouse (Invitrogen, Molecular Probes, no. A-11029) and were diluted 1:200. F-actin was stained with phalloidin-TRITC (Sigma-Aldrich, no. P1951) and was diluted 1:1,000.

**Time-lapse microscopy.** Multidimensional acquisitions were performed on an automated inverted microscope (Nikon Eclipse Ti, ×10 lens) equipped with thermal, CO<sub>2</sub> and humidity control, using MetaMorph (Universal Imaging) software. Images were obtained every 3 min during 450 min. Up to 15 independent monolayers were imaged in parallel using a motorized XY stage.

**Particle imaging velocimetry and strain rate calculation.** Monolayer velocity fields were computed using a custom-made particle imaging velocimetry software. To reduce systematic biases in subpixel resolution and peak-locking effects, we implemented an iterative process (up to 4 iterations) based on a continuous window shift technique<sup>13</sup>.

Strain rate  $\epsilon_{xx}^{\dot{}}$  was calculated using the following expression<sup>13,65</sup>:

$$\epsilon_{xx}^{\dot{}} = \frac{dV_x}{dx}$$

**Traction force microscopy.** Traction forces were computed using Fourier-transform traction microscopy with finite gel thickness<sup>66</sup>. Gel displacements between any experimental time point and a reference image obtained after cell trypsinization were computed using the particle imaging velocimetry software described above.

**Monolayer stress microscopy.** In a two-dimensional approximation, monolayer stress is fully captured by a tensor possessing two independent normal components ( $\sigma_{xx}$  and  $\sigma_{yy}$ ) and two identical shear components ( $\sigma_{xy}$  and  $\sigma_{yx}$ ; refs 6,14,33). At every pixel of the monolayer, these four components of the stress tensor define two particular directions of the plane, one in which the normal stress is maximum and one in which it is minimum. These directions, which are mutually orthogonal, are called principal stress orientations, and the stress values in each principal orientation are called maximum ( $\sigma_{11}$ ) and minimum ( $\sigma_{22}$ ) stress components. The average normal stress is defined as  $\sigma_n = (\sigma_{11} + \sigma_{22})/2$ , and the maximum shear stress is defined as  $\sigma_s = (\sigma_{11} - \sigma_{22})/2$ . The spatial resolution and force precision of MSM are formally set by those in the original traction maps. How the reconstructed stress field is affected by the choice of boundary conditions and by the assumptions of continuity, incompressibility and homogeneity was extensively studied elsewhere<sup>13,34</sup>.

**Magnetocytometry.** Bead pulling experiments were performed using magnetic tweezers as previously described<sup>47,66</sup>. Briefly, 3-µm-diameter magnetic beads pre-coated with protein G (Novex) were covalently coated with purified E-cadherin-Fc or P-cadherin-Fc proteins. Unless noted otherwise, the beads were first washed with Na phosphate buffer (0.1 M, pH 8), incubated with 20 µg ml<sup>-1</sup> of the Fc-tagged proteins for 2 h, and then with crosslinking buffer for 1 h (25 mM DMP, 0.2 M triethanolamine, pH 8.2). The protein-coated beads were allowed to settle on a confluent monolayer of MCF10A cells for 30 min before starting the experiment. To measure the extent of reinforcement, a pulsatory force (0.2 nN unless stated otherwise) was applied to beads attached to cells. Bead movement in response to the pulsatory force was tracked using a custom-made tracking software. Stiffness of the cell-bead contact was calculated as the ratio between the amplitude of the applied force and that of the observed bead oscillation. The magnetic force generated by the magnet is restricted to the close proximity of the magnet tip<sup>47,66</sup>. All beads probed from one sample were selected far enough from each other so that they experienced the forcing protocol only once.

Vinculin recruitment was measured using magnetic twisting cytometry as previously described<sup>50</sup>.

**Averaging.** Physical properties of cells and cell monolayers often exhibit broad non-Gaussian distributions with log-normal or exponential tails<sup>67</sup>. To avoid potential averaging artefacts caused by extreme data in these tails, we first computed the median—rather than the mean—of any physical property across space (Supplementary Note). We then averaged medians over experimental repeats and/or time. In the case of cell velocities, which average to roughly zero owing to the symmetry of monolayer expansion, we computed the median of absolute values.

**Computation of  $z$ -scores.** The  $z$ -score (or standard score in statistics) is defined as the signed number of standard deviations an observed quantity deviates from the mean of that quantity<sup>68</sup>. In the context of this study, the  $z$ -score of a quantity  $x$  (a physical property in Fig. 5a or a protein concentration in Fig. 6a) in response to a siRNA perturbation is defined as:

$$z = \frac{\bar{x} - \bar{x}_c}{\sigma_c}$$

where  $\bar{x}$  is the mean of  $x$  under the siRNA perturbation,  $\bar{x}_c$  is the mean of  $x$  under control conditions, and  $\sigma_c$  is the standard deviation of  $x$  under control conditions.

**Computation of correlation matrices.** As a measure of correlation we used cosine similarity between pairs of vectors containing  $z$ -scores of physical properties. Consider a matrix  $Z$  containing the  $z$ -scores of  $n$  physical properties under  $m$  siRNA perturbations ( $m$  rows and  $n$  columns). Each column of the matrix defines an  $m$ -dimensional vector  $\mathbf{P}$  that contains the  $z$ -scores of one physical property. To assess the correlation between two physical properties  $i$  and  $j$  we computed the cosine of the angle  $\theta_{ij}$  between the vectors  $\mathbf{P}_i$  and  $\mathbf{P}_j$  (vectors that contain the  $z$ -scores of properties  $i$  and  $j$ ):

$$\cos(\theta_{ij}) = \frac{\mathbf{P}_i \mathbf{P}_j}{\|\mathbf{P}_i\| \|\mathbf{P}_j\|}$$

When repeated over each possible pair of physical properties, this operation yields an  $n \times n$  correlation matrix  $C$  in which each element is defined as  $C_{ij} = \cos(\theta_{ij})$ . This matrix is shown in Fig. 5b. In a similar way, we also computed a  $q \times q$  correlation matrix of siRNA perturbations (Fig. 5c) and a  $k \times k$  correlation matrix of protein concentrations (Fig. 6b).

**Unsupervised clustering analysis.** Unsupervised clustering analysis was performed as described previously<sup>41</sup> (see also Supplementary Note). Briefly, we first ordered the correlation matrix to place high correlation values close to the diagonal and low correlation values close to the matrix edges. Second, we obtained clusters by identifying diagonal blocks containing elements of high correlation. To this end, we assumed a matrix model that is block diagonal in which matrix elements in each block are equal and off-diagonal elements are also equal. We then obtained the

block diagonal model that fits best our ordered matrix according to the Bayesian information criterion.

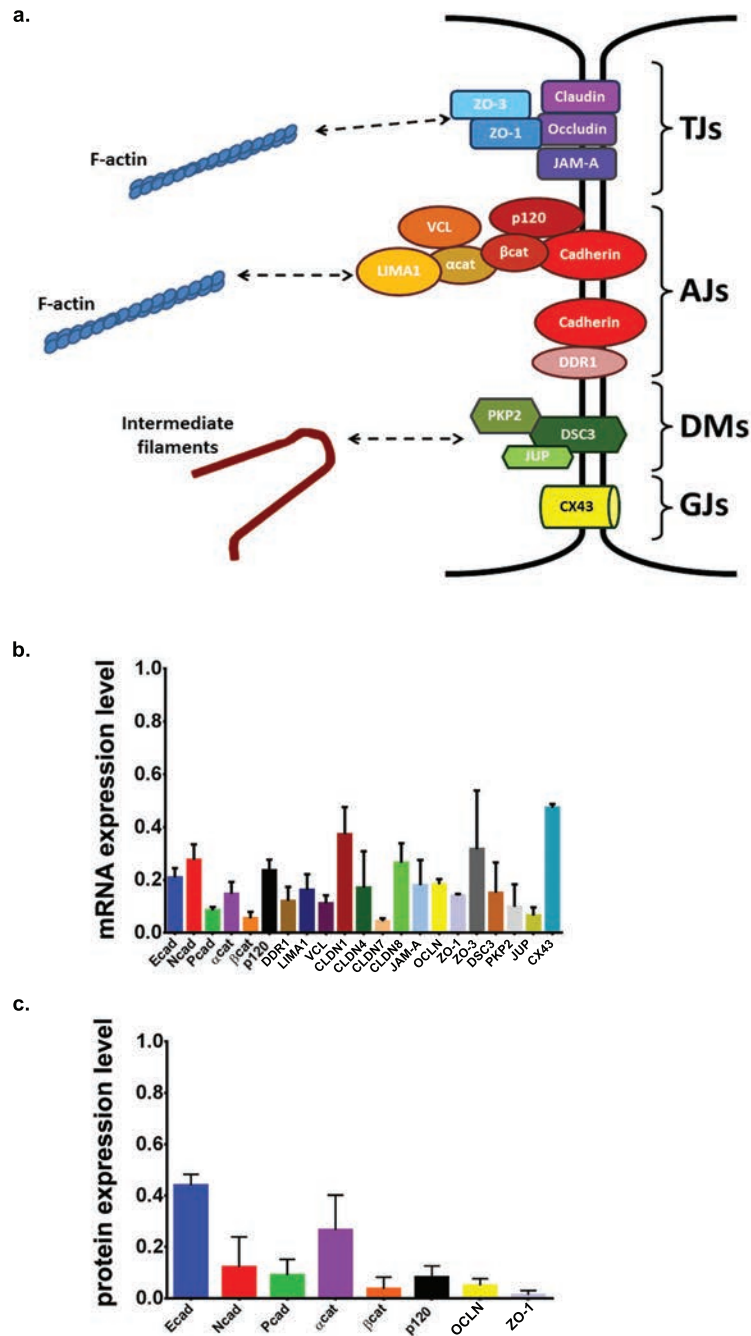
**Leave-one-out cross-validation.** To select predictive models and assess their predictive power we performed a LOOCV analysis<sup>69</sup>. We proceeded as follows. For a given physical property  $X$  and a given silencing condition  $k$ , we fit the linear model (equation (1) for one protein, or a linear combination of  $N$  proteins for  $N$ -protein models) using the values of  $X$  under all conditions except  $k$  (that is, we determine  $A$  and  $B$ , leaving condition  $k$  out). Then we used the fitted model to make a prediction of  $X$  under condition  $k$ . We repeated the same operation for all conditions and computed the mean squared error of the predictions. The most predictive model was then the one that yielded the smallest mean squared error. To establish significance of the predictions and ensure that low prediction errors were not merely an outcome of multiple testing, we ran randomization tests on the values of the physical properties and kept only models whose prediction error was significantly low at a 5% level. This approach is typically used to avoid overfitting when the number of potential explanatory variables (in our case, protein concentrations) is of the order of the number of conditions (in our case, siRNAs) under which predictions are sought.

**Code availability.** Computer codes developed for this study can be made available on request to the corresponding author.

**Repeatability of experiments.** All immunostaining experiments were performed on at least three independent cell culture preparations, imaged over two or more imaging sessions. Magnetic tweezers experiments were performed in three independent cell culture preparations. Western blot experiments were performed on three independent transfections. Real-time PCR experiments were run in triplicate and performed on at least two independent transfections.

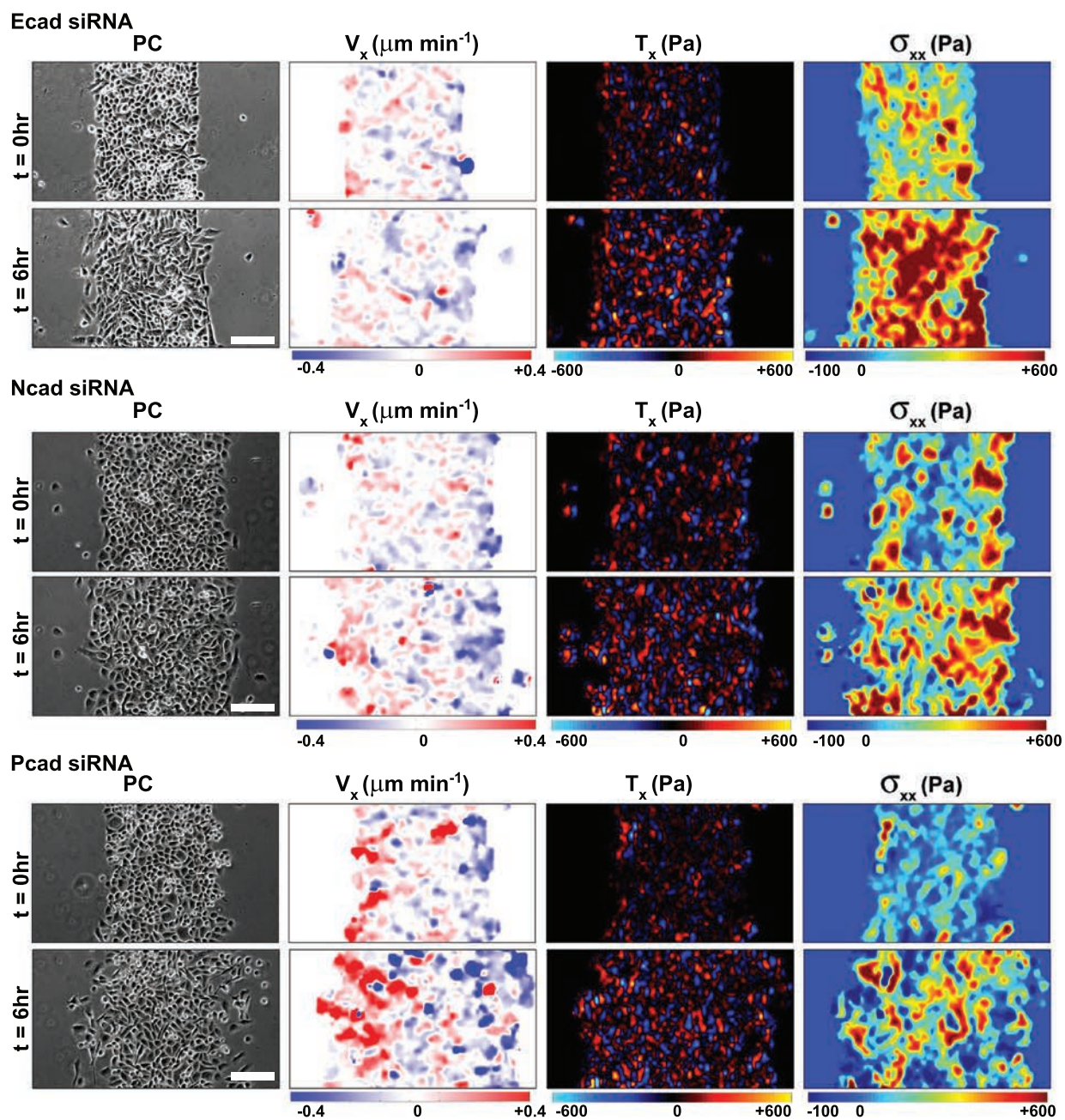
62. Kandow, C. E., Georges, P. C., Janmey, P. A. & Beningo, K. A. Polyacrylamide hydrogels for cell mechanics: steps toward optimization and alternative uses. *Methods Cell Biol.* **83**, 29–46 (2007).
63. Yeung, T. *et al.* Effects of substrate stiffness on cell morphology, cytoskeletal structure, and adhesion. *Cell. Motil. Cytoskeleton* **60**, 24–34 (2005).
64. Ostuni, E., Kane, R. S., Chen, C. S., Ingber, D. E. & Whitesides, G. M. Patterning mammalian cells using elastomeric membranes. *Langmuir* **16**, 7811–7819 (2000).
65. Blanchard, G. B. *et al.* Tissue tectonics: morphogenetic strain rates, cell shape change and intercalation. *Nat. Methods* **6**, 458–464 (2009).
66. Roca-Cusachs, P. *et al.* Integrin-dependent force transmission to the extracellular matrix by  $\alpha$ -actinin triggers adhesion maturation. *Proc. Natl Acad. Sci. USA* **110**, E1361–E1370 (2013).
67. Fabry, B. *et al.* Time scale and other invariants of integrative mechanical behavior in living cells. *Phys. Rev.* **68**, 041914 (2003).
68. Birmingham, A. *et al.* Statistical methods for analysis of high-throughput RNA interference screens. *Nat. Methods* **6**, 569–575 (2009).
69. Simon, R. in *Fundamentals of Data Mining in Genomics and Proteomics* (eds Dubitzky, W., Granzow, M. & Berrar, D. P.) 177–178 (Springer Science+Business Media, 2007).

DOI: 10.1038/ncb3135



**Supplementary Figure 1** mRNA and protein expression levels after siRNA transfections. (a) Scheme illustrating the localization of all targeted proteins. (b) Levels of mRNA after 5 days of transfection. Data were quantified by RT-PCR. Data are presented as mean ± SEM (normalized to control cells). RT-PCR was run in triplicate. n=12 samples pooled from 4 independent experiments for CT siRNA, Ncad siRNA, Pcad siRNA, DSC3 siRNA, αcat siRNA, p120 siRNA, LIMA1 siRNA, CLDN8 siRNA, JAM-A siRNA; n=9

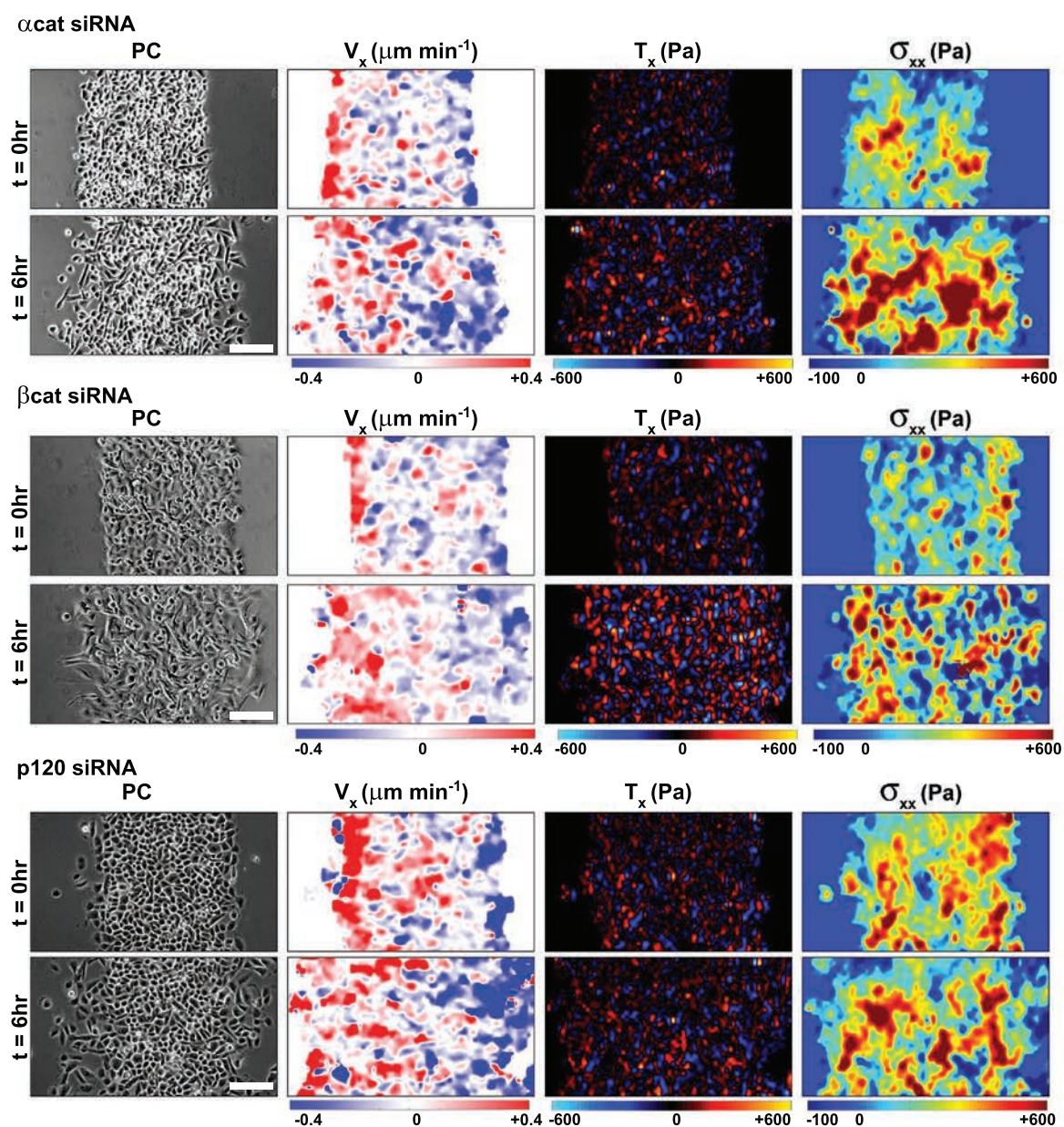
samples pooled from 3 independent experiments for βcat siRNA, DDR1 siRNA, VCL siRNA, CLDN1 siRNA, CLDN7 siRNA, ZO-1 siRNA, ZO-3 siRNA, PKP2 siRNA, JUP siRNA; n=6 samples pooled from 2 independent experiments for CLDN4 siRNA, CX43 siRNA, OCLN siRNA. (c) Protein levels after 5 days of transfection. Data are presented as mean ± SEM. For each protein, n=3 samples pooled from 3 independent transfections (normalized to control cells).



**Supplementary Figure 2** Representative maps of monolayer mechanics for siRNA perturbations targeting E-, N-, and P-cadherin. Data show phase contrast images (first column), velocities in the x direction (second column),

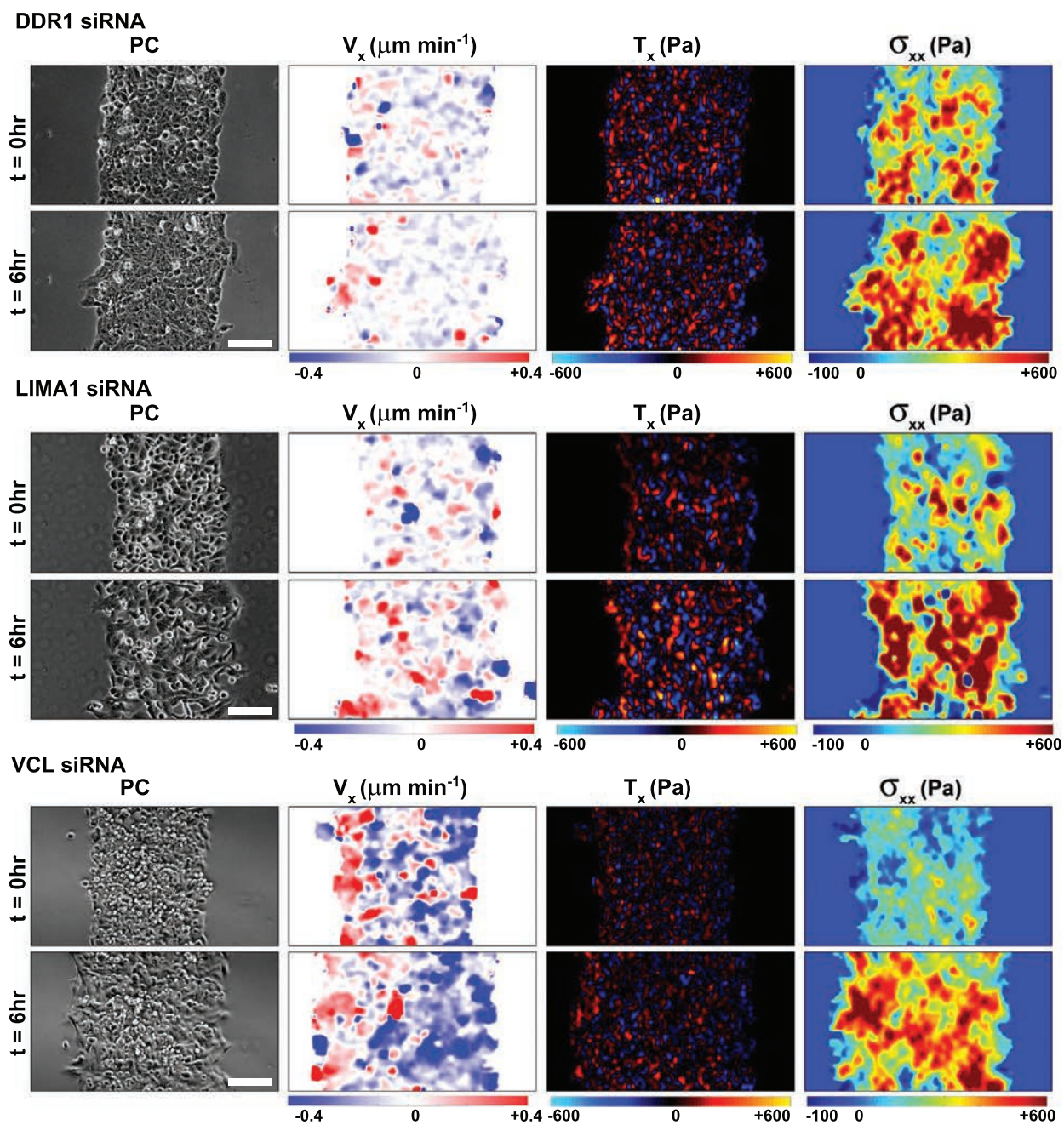
traction forces in the x direction (third column), and monolayer tension (fourth column) for two time points (0h first row and 6h second row). Scale bar, 100 $\mu\text{m}$ .





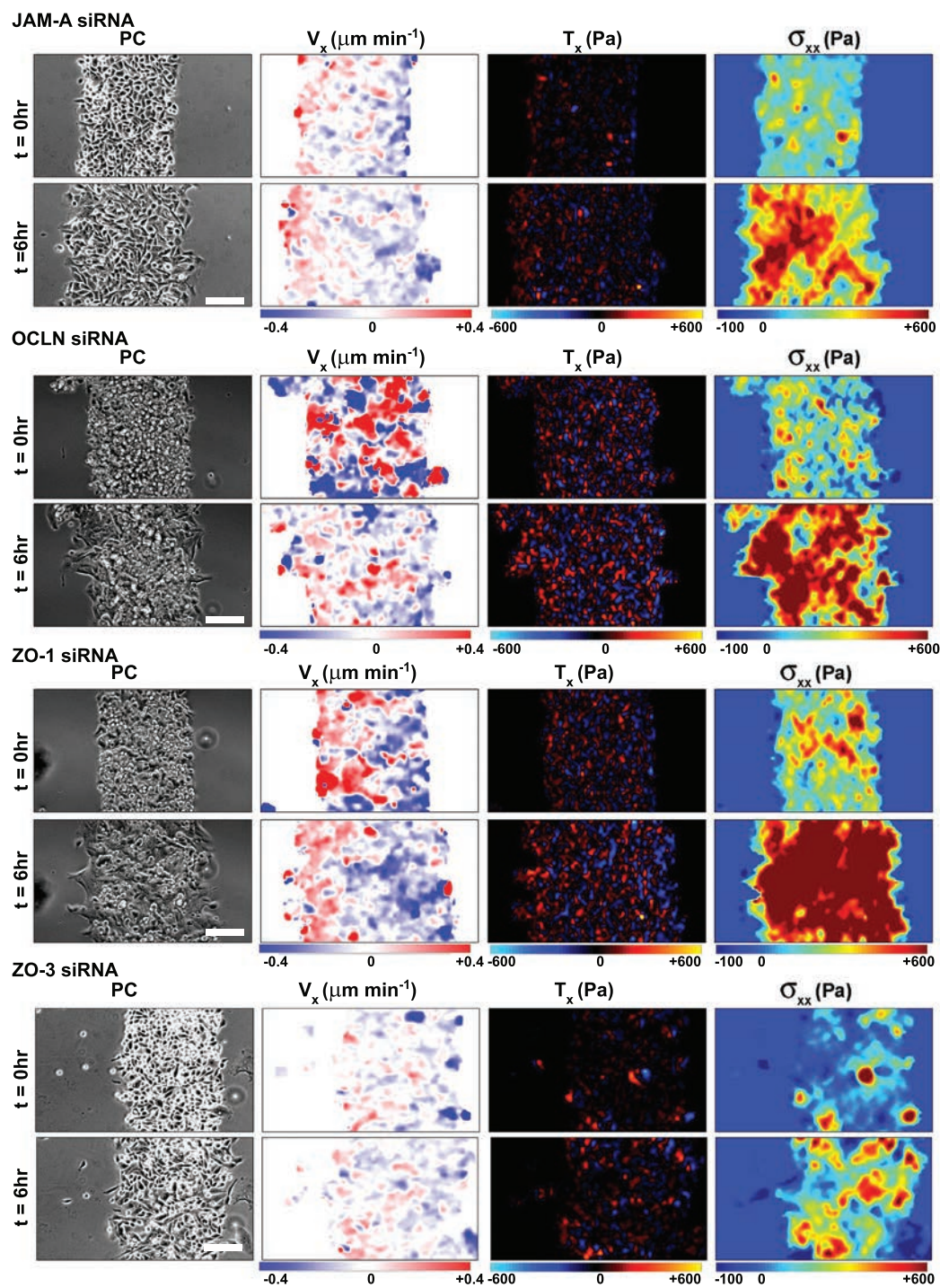
**Supplementary Figure 3** Representative maps of monolayer mechanics for siRNA perturbations targeting  $\alpha$ -catenin,  $\beta$ -catenin, and p120. Data show phase contrast images (first column), velocities in the x direction (second

column), traction forces in the x direction (third column), and monolayer tension (fourth column) for two time points (0h first row and 6h second row). Scale bar, 100 $\mu$ m.



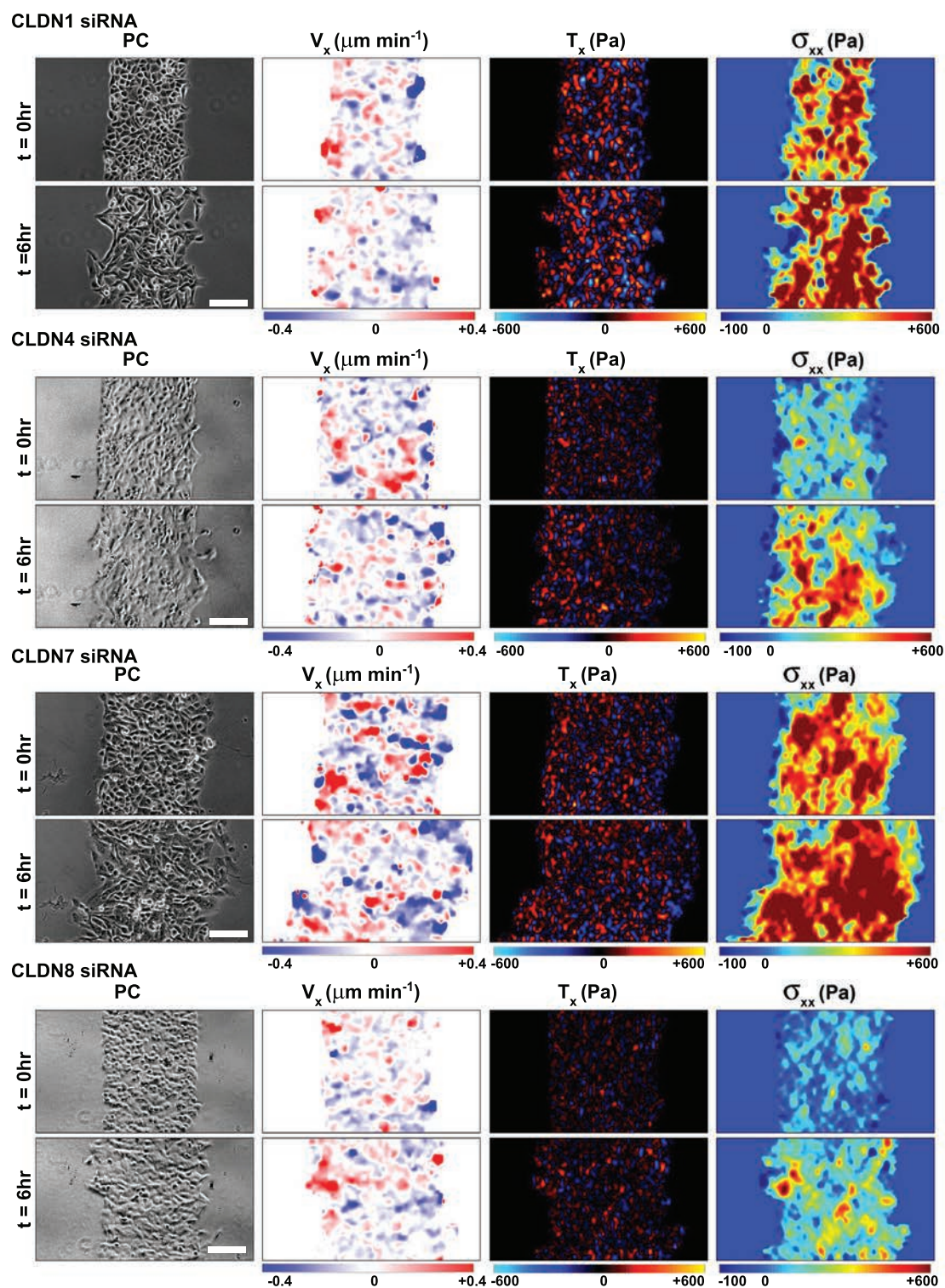
**Supplementary Figure 4** Representative maps of monolayer mechanics for siRNA perturbations targeting DDR1, LIMA1, and VCL. Data show phase contrast images (first column), velocities in the x direction (second column),

traction forces in the x direction (third column), and monolayer tension (fourth column) for two time points (0h first row and 6h second row). Scale bar, 100 $\mu$ m.



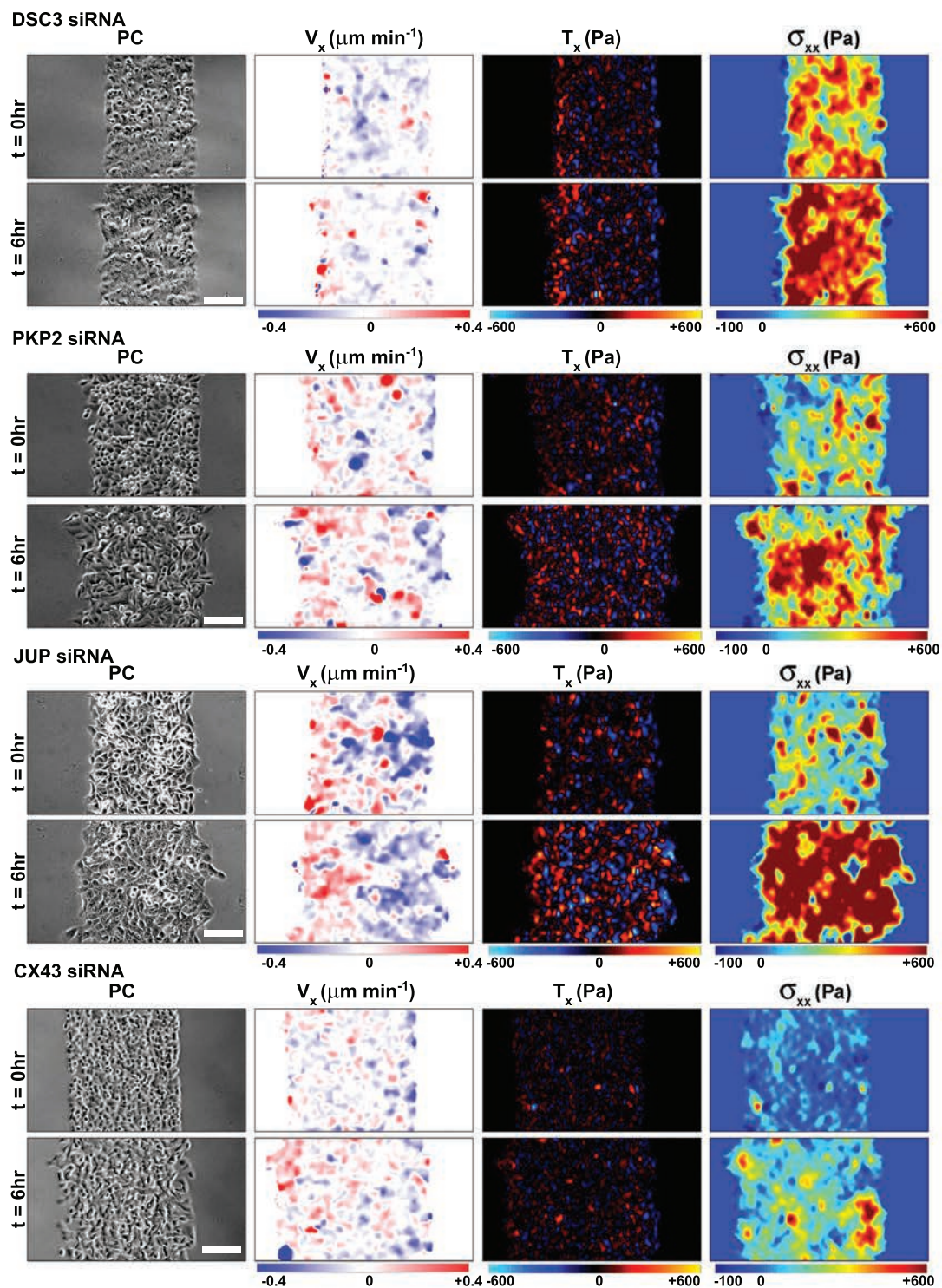
**Supplementary Figure 5** Representative maps of monolayer mechanics for siRNA perturbations targeting JAM-A, OCLN, ZO-1, and ZO-3. Data show phase contrast images (first column), velocities in the x direction (second

column), traction forces in the x direction (third column), and monolayer tension (fourth column) for two time points (0h first row and 6h second row). Scale bar, 100μm.



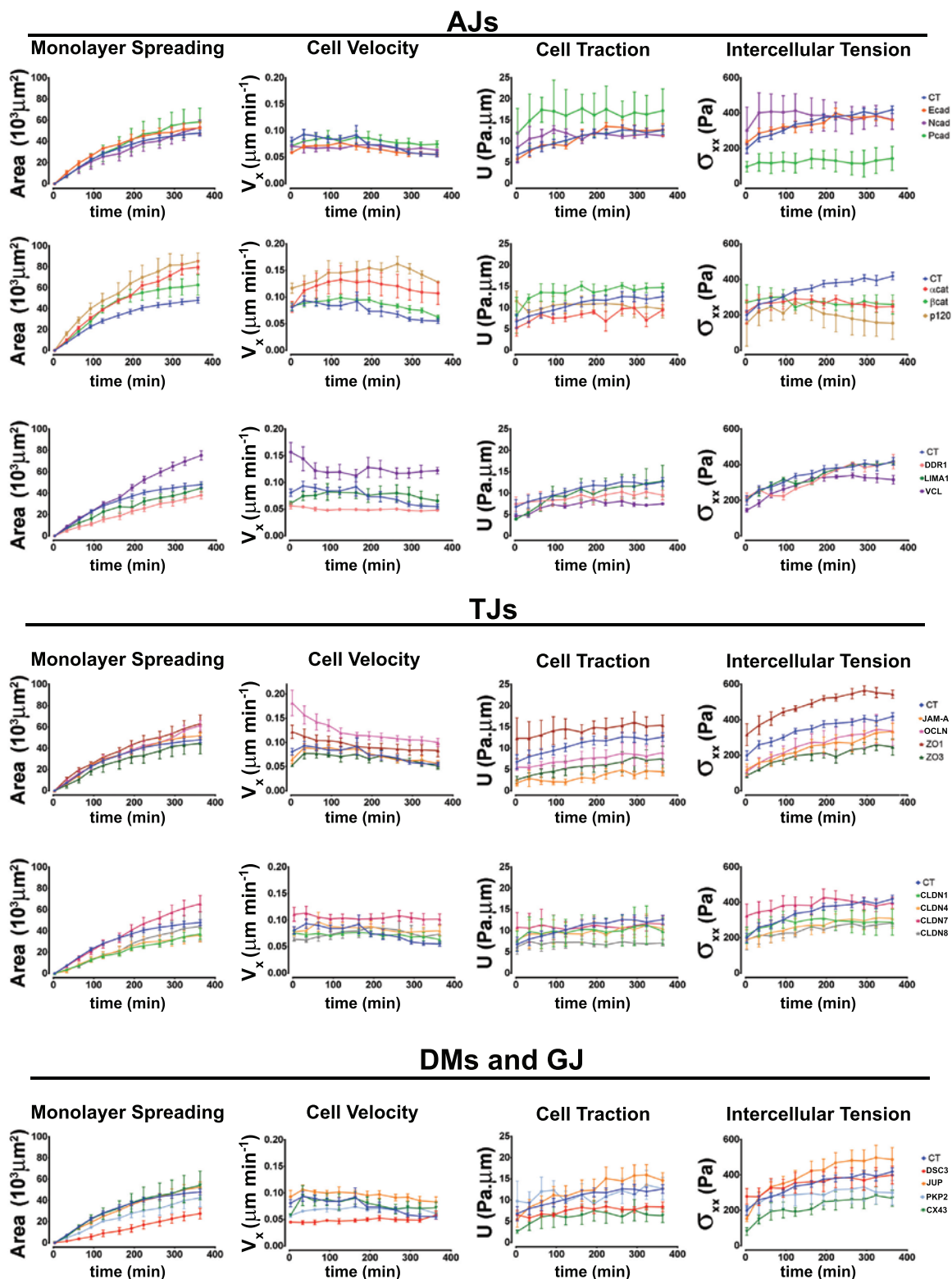
**Supplementary Figure 6** Representative maps of monolayer mechanics for siRNA perturbations targeting claudins 1, 4, 7, and 8. Data show phase contrast images (first column), velocities in the x direction (second column),

traction forces in the x direction (third column), and monolayer tension (fourth column) for two time points (0h first row and 6h second row). Scale bar, 100μm.



**Supplementary Figure 7** Representative maps of monolayer mechanics for siRNA perturbations targeting desmocollin 3, plakophilin 2, plakoglobin, and connexin 43. Data show phase contrast images (first column), velocities

in the x direction (second column), traction forces in the x direction (third column), and monolayer tension (fourth column) for two time points (0h first row and 6h second row). Scale bar, 100 $\mu\text{m}$ .



**Supplementary Figure 8** Time evolution of monolayer mechanics for each siRNA perturbation. Data are presented as mean  $\pm$  SEM.  $n=13$  independent cell monolayers (CT siRNA),  $n=3$  independent cell monolayers (Ecad siRNA,  $\beta$ cat siRNA, JAM-A siRNA, ZO-3 siRNA, Ncad siRNA, LIMA1 siRNA, DDR1 siRNA, PKP2 siRNA),  $n=4$  independent cell monolayers (Pcad siRNA,  $\alpha$ cat siRNA, p120 siRNA, CX43 siRNA, VCL siRNA, JUP siRNA),  $n=5$  independent cell monolayers (DSC3 siRNA, CLDN1 siRNA, CLDN8 siRNA),  $n=6$  independent monolayers (OCLN

siRNA, CLDN4 siRNA),  $n=7$  independent cell monolayers (ZO-1 siRNA),  $n=8$  independent cell monolayers (CLDN7 siRNA); monolayers were assessed from 10 experiments (CT siRNA), 4 experiments (CLDN7 siRNA, CLDN4 siRNA), 3 experiments ( $\alpha$ cat siRNA, CX43 siRNA, DSC3 siRNA), 2 experiments (Ecad siRNA,  $\beta$ cat siRNA, JAM-A siRNA, ZO-3 siRNA, Ncad siRNA, LIMA1 siRNA, DDR1 siRNA, PKP2 siRNA, Pcad siRNA, p120 siRNA, VCL siRNA, JUP siRNA, CLDN1 siRNA, CLDN8 siRNA, OCLN siRNA, ZO-1 siRNA).

Variable	Definition	Description	Technique	Units
$T_x$	Traction force in the $x$ direction	Force per unit area exerted by cells on the underlying substrate along the $x$ -axis.	TM	Pa
$T_y$	Traction force in the $y$ direction	Force per unit area exerted by cells on the underlying substrate along the $y$ -axis.	TM	Pa
$U$	Strain energy density	Energy per unit area transferred by cells to the substrate.	TM	Pa· $\mu\text{m}$
$\sigma_{xx}$	Normal component of the stress tensor in the $x$ direction	Force per unit cross-sectional area acting in the direction normal to the $yz$ plane ( $x$ direction, i.e. direction of monolayer expansion). In this study $\sigma_{xx}$ was termed monolayer tension or intercellular tension.	MSM	Pa
$\sigma_{yy}$	Normal component of the stress tensor in the $y$ direction.	Force per unit cross-sectional area acting in the direction normal to the $xz$ plane ( $y$ direction, i.e. direction perpendicular to that of monolayer expansion).	MSM	Pa
$\sigma_{xy}$	Shear component of the stress tensor	Force per unit cross-sectional area acting in the direction parallel to the $yz$ plane.	MSM	Pa
$\sigma_{yx}$	Shear component of the stress tensor	Force per unit cross-sectional area acting in the direction parallel to the $xz$ plane. $\sigma_{yx}$ is equal to $\sigma_{xy}$ .	MSM	Pa
$\sigma_{11}$	Maximum principal stress	Maximal force per unit cross-sectional area.	MSM	Pa
$\sigma_{22}$	Minimum principal stress	Minimal force per unit cross-sectional area.	MSM	Pa
$\sigma_n$	Average normal stress	$\sigma_n = (\sigma_{11} + \sigma_{22}) / 2$	MSM	Pa
$\sigma_s$	Maximum shear stress	$\sigma_s = (\sigma_{11} - \sigma_{22}) / 2$	MSM	Pa
$\sigma_{xx}^f$	Final normal stress in the $x$ direction	Value of $\sigma_{xx}$ at the end of the experiment.	MSM	Pa
$\dot{\sigma}_{xx}$	Stress rate	Rate at which $\sigma_{xx}$ evolves during an experiment. It was obtained by fitting a first order polynomial to the time evolution of $\sigma_{xx}$ .	MSM	Pa/hr
$\sigma_{xx}^m$	Time-averaged normal stress in the $x$ direction	Average of $\sigma_{xx}$ over time, space, and experimental repeats.	MSM	Pa
$V_x$	Velocity in the $x$ direction	Local velocity in each pixel of the monolayer in the $x$ direction.	PIV	$\mu\text{m}/\text{min}$
$V_y$	Velocity in the $y$ direction	Local velocity in each pixel of the monolayer in the $y$ direction.	PIV	$\mu\text{m}/\text{min}$
$V_i$	Instantaneous cell velocity	Cell velocity between two consecutive time points	Cell Tracking	$\mu\text{m}/\text{min}$
$V_e$	Euclidean velocity	Euclidian distance between the initial and final cell positions divided by the recording time	Cell Tracking	$\mu\text{m}/\text{min}$
$\epsilon_{\dot{\lambda}xx}$	Normal component of the strain rate tensor	Rate at which the monolayer is stretching or compressing in the $x$ direction. $\epsilon_{\dot{\lambda}xx} = \frac{d\lambda_{xx}}{\lambda_{xx} dt}$		$\text{min}^{-1}$
$\Delta A$	Increase in monolayer area	Difference between the area of the monolayer at time $t$ and its initial value.	PC	$\mu\text{m}^2$

**Supplementary Table 1. List of all physical variables measured or computed in this study.** We also list their definition, a short description, the technique used to measure them, and their units. TM (traction microscopy), MSM (monolayer stress microscopy), PIV (particle imaging velocimetry), PC (phase contrast).

$\sigma_{\text{cad}}^{\text{ml}}$	52.45	1	Pcad
$\sigma_{\text{cad}}^{\text{f}}$	74.22	1	Pcad
$\sigma_{\text{cad}}^{\text{e}}$	17.02	1	Ecad

**Supplementary Table 2. List of all 1-protein models that predict physical properties with statistical significance ( $p < 0.05$ , leave-one-out cross-validation).** The first column indicates the physical property predicted (only physical properties that yielded significant predictions are listed). The second column contains the prediction error (mean standard error) in units of the physical quantity predicted. The third column contains the number of proteins in the model (in this case 1). The fourth column contains the proteins involved in the linear model.



SUPPLEMENTARY INFORMATION

$\sigma_{xxx}^{m}$	51.99	2	Pcad	$\beta$ cat			
	52.30	2	Pcad	p120			
	52.45	1	Pcad				
	52.78	4	Ncad	Pcad	$\alpha$ cat	p120	
	52.87	3	Pcad	$\beta$ cat	p120		
	53.36	2	Pcad	$\alpha$ cat			
	53.47	3	Pcad	$\alpha$ cat	p120		
	55.06	2	Ecad	Pcad			
	55.12	5	Ncad	Pcad	$\beta$ cat	$\alpha$ cat	p120
	55.19	3	Ncad	Pcad	$\beta$ cat		
	55.45	3	Ecad	Pcad	$\beta$ cat		
	56.36	2	Ncad	Pcad			
	56.85	3	Ecad	Pcad	$\alpha$ cat		
	57.23	3	Ncad	Pcad	p120		
	57.61	4	Ncad	Pcad	$\beta$ cat	p120	
	57.75	5	Ecad	Ncad	Pcad	$\alpha$ cat	p120
	57.91	3	Ecad	Pcad	p120		
	58.69	4	Ecad	Pcad	$\beta$ cat	p120	
	58.72	4	Ecad	Ncad	Pcad	$\alpha$ cat	
	59.14	3	Ncad	Pcad	$\alpha$ cat		
	59.39	4	Ecad	Ncad	Pcad	$\beta$ cat	
	59.44	3	Ecad	Ncad	Pcad		
	60.06	3	Pcad	$\beta$ cat	$\alpha$ cat		
	60.18	4	Ecad	Pcad	$\alpha$ cat	p120	
60.75	6	Ecad	Ncad	Pcad	$\beta$ cat	$\alpha$ cat	p120
61.77	4	Ecad	Ncad	Pcad	p120		
61.87	4	Pcad	$\beta$ cat	$\alpha$ cat	p120		
$\sigma_{xxx}^f$	63.65	3	Ecad	Pcad	$\beta$ cat		
	64.29	3	Pcad	$\beta$ cat	p120		
	65.42	4	Ecad	Pcad	$\beta$ cat	p120	
	68.16	2	Ecad	Pcad			
	68.22	5	Ecad	Ncad	Pcad	$\beta$ cat	p120
	68.91	2	Pcad	$\beta$ cat			
	70.57	4	Ecad	Ncad	Pcad	$\beta$ cat	
	71.58	3	Ecad	Pcad	p120		
	71.83	2	Pcad	p120			
	71.86	4	Ncad	Pcad	$\beta$ cat	p120	
	72.40	3	Ecad	Ncad	Pcad		
	72.67	4	Pcad	$\beta$ cat	$\alpha$ cat	p120	
	73.46	4	Ecad	Ncad	Pcad	p120	
	73.52	3	Ecad	Pcad	$\alpha$ cat		
	73.69	3	Pcad	$\alpha$ cat	p120		
	74.22	1	Pcad				
	74.46	3	Ncad	Pcad	p120		
	76.08	3	Pcad	$\beta$ cat	$\alpha$ cat		
	77.05	2	Pcad	$\alpha$ cat			
	77.40	4	Ecad	Pcad	$\alpha$ cat	p120	
$\sigma_{xxx}^r$	10.31	4	Pcad	$\beta$ cat	$\alpha$ cat	p120	
	11.32	5	Ecad	Pcad	$\beta$ cat	$\alpha$ cat	p120
	11.80	5	Pcad	$\beta$ cat	$\alpha$ cat	p120	ZO1
	12.06	4	Ecad	Pcad	$\beta$ cat	$\alpha$ cat	
	12.09	3	Pcad	$\beta$ cat	$\alpha$ cat		
13.23	6	Ecad	Pcad	$\beta$ cat	$\alpha$ cat	p120	ZO1

**Supplementary Table 3: List of all N-protein models that predict physical properties with statistical significance ( $p < 0.05$ , leave-one-out cross-validation).** The first column indicates the physical property predicted (only physical properties that yielded significant predictions are listed). The second column contains the prediction error (mean standard error) in units of the physical quantity predicted. The third column contains the number of proteins in the model. The fourth column contains the proteins involved in the linear model.

Protein	Gene	siRNA	Sequences (5'-----3')	Taqman probe
E-cadherin	<i>CDH1</i>	s2768	GAACUUAUUUUCUUGUGAAtt	Hs 01013959_m1
		s2769	CAACAGCUGUGAUCACAGUtt	
		s2770	CGUAUACCCUGGUGUUAAtt	
N-cadherin	<i>CDH2</i>	s2771	GUGCAACAGUAUACGUUAAtt	Hs00169953_m1
		s2772	GGGUAAUCCUCCAAAUCAtt	
		s2773	GAACAUUUGUGAUGACCGUtt	
P-cadherin	<i>CDH3</i>	s2774	CACUGAUUGAUGUCAUUGAAtt	Hs00354998_m1
		s2775	CCUCUUGUGUUCGACUAtt	
		s2776	CAAGAUUACGAUUUUCUGAAtt	
cc-catenin	<i>CTNNA1</i>	s3716	GUGGAUAAGCUGAACAUUAtt	Hs 00944794_m1
		s3717	GUGUAAAAGCUUUGUCGAAUtt	
		s3718	CUACGUCGCCUCUACCAAAAtt	
β-catenin	<i>CTNNB1</i>	s436	GGACCUAUACUUCAGAAAAtt	Hs00355049_m1
		s437	GGAUUUCACACCGGAUUtt	
		s438	CUGUUGGAUUGAUUCGAAAAtt	
p120	<i>CTNND1</i>	s3725	GCUCGCAACAAGAAUUAAtt	Hs00931670_m1
		s3726	CAUUGACCCGGAACAAAAtt	
		s3727	GAACUUUAUCAUAUAAAGUtt	
LIMA1	<i>LIMA 1</i>	s224214	GGAGAAUGAGAAUCUUGUAtt	Hs00212557_m1
		s224215	GGCUAAAGUAGUUGUUGAtt	
		s28189	GUGAGGAUCUUAAGACCAAtt	
DDR1	<i>DDR1</i> Dharmacon	D-003111-10	GAAUGCGCUCCGGCGUGUU	Hs01058430_m1
		D-003111-10	GAGCGUCUGUCGCGGUAUU	
Vinculin	<i>VCL</i>	s14762	GGUUGGUACUGUAAUAAAAtt	Hs00419715-m1
		s14763	GCUUCAAUCAAUUUCGAAtt	
		s14764	GCUCGUAUCUUACUUAAGGAtt	
Claudin 1	<i>CDLN1</i>	s17315	CAAUAGAAUCGUUCAAGAAtt	Hs00221623_m1
		s17316	GACUCCUUGCUGAAUCUGAtt	
		s17317	ACCUCUUACCCAACCAAtt	
Claudin 4	<i>CLDN4</i>	s3441	ACAUCAUCCAAGACUUCUAtt	Hs00533616_s1
		s3442	CCCUCGUAUCAUCAGCAUtt	
		s223316	UCUGUUUGUAUUUAAGAtt	
Claudin 7	<i>CLDN7</i>	s3447	CAGACUUUUUAACCCUUtt	Hs00600772_m1
		s3448	CCCUACCAACAUUAAGUAUtt	
		s223318	UGAUGAGCUGCAAAUUGUAtt	
Claudin 8	<i>CLDN8</i>	s17306	CCAUCGCACAACCAAAAAtt	Hs00273282_s1
		s17307	CAACAUCGUGGUUUUGAAtt	
		s17308	UAGUGAAUGUUGCCAAAAtt	
ZO-1	<i>TJP1</i>	s14155	GGUUGUUUUCGUCGCAUtt	Hs00543824_m1
		s14156	CGAUCUCAUAAACUUCGUAtt	
		s14157	CUGUCAUACUUUGACCGAAtt	
ZO-3	<i>TJP3</i>	s25885	GCGACUGAUUGAGAAGUCAAtt	Hs00274276_m1
		s25886	GGAGAUUCUAUUCACAGAtt	
		s25887	GGACAGCAUGCGAACCUAAtt	
Occludin	<i>OCN</i>	s9812	CCUUUUAGGAGGUGAGUAtt	Hs00170162_m1
		s9813	CCGAAUCAUUUUGCACCAtt	
		s9814	CUACUUAAGUGUGAUAAUAtt	
JAM-A	<i>F11R</i>	s27150	GCCUAGUCCCGAAGUGAAtt	Hs00170991_m1
		s27151	CCAUCCAAGCCUACAGUUAtt	
		s27152	GGAUAGUGAUGCCUACGAAtt	
DSC3	<i>DSC3</i>	s4312	GACGUGGAGUUGAUAAAGAtt	Hs00170032_m1
		s4313	CCCAAUAUGUGCGGAUUAAtt	
		s4314	GAUCAACGGCUUAAGGCAAtt	
JUP	<i>JUP</i>	s7666	CUCUGGCGUCUACUAUtt	Hs00158408_m1
		s7667	CCAUCGGCUUGAUCAGGAAtt	
		s7668	GAUCAUGCGUAACUACAGUtt	
PKP2	<i>PKP2</i>	s10583	CCAGAAUAUCUAUUAUCAAtt	Hs00428040_m1
		s10584	GAAGCAUUGCUUACGCGUAtt	
		s10585	CAGCUACUUUCAUCAGCAtt	
CX43	<i>GJA1</i>	s5757	ACUAGCUGCUGGACAUGAAtt	Hs00748445_s1
		s5758	GGCUAAUUACAGUCAGAAtt	
		s5759	GAACCUACAUCAUCAGUAUtt	
	CT Negative control	4390843		Taqman control s18 Hs01584357-g1

**Supplementary Table 4. List of siRNAs used for this study with their corresponding Taqman probes.** All siRNAs were obtained from Life Technologies except for *DDR1*, which was obtained from Dharmacon. All Taqman probes were obtained from Applied Biosystems.



**Supplementary Videos Legends**

**Supplementary Video 1: Expansion of a micropatterned monolayer of MCF10A cells.** Scale bar, 100 $\mu$ m.

**Supplementary Video 2: Dynamics of an expanding cell monolayer of MCF10A cells.** Top: velocity field  $V_x$  overlaid on phase contrast images. Middle: traction force field  $T_x$  overlaid on phase contrast images. Bottom: monolayer tension overlaid on phase contrast images. Scale bar, 100 $\mu$ m.

**Supplementary Video 3: Time evolution of monolayer tension in response to siRNAs targeting cell-cell junctions.** Composition of representative experiments for the 21 siRNA pools and 3 controls. Each panel shows monolayer tension overlaid on phase contrast images. Scale bar, 100 $\mu$ m.

# Supplementary Note

## 1) Unsupervised clustering analysis

The method we use follows the approach developed by Sales-Pardo et al<sup>1</sup>. It has three different steps:

1. Building the correlation matrix;
2. Ordering the correlation matrix;
3. Identifying the clusters.

### Building the correlation matrix

Consider a table  $T$  with  $R$  rows corresponding to experimental conditions and  $C$  columns corresponding to experimental observables. In our case,  $T$  is the matrix of z-scores with respect to the control condition (see main text). For each table we obtain two correlation matrices: one for the columns and one for the rows.

For clarity let's consider the correlation matrix  $A$  obtained for the rows in matrix  $T$ . For each row  $i$ , we define a vector  $\mathbf{T}_i = (T_{i1}, \dots, T_{iC})$  with the matrix elements in that row. Then, we assign to each element  $A_{ij}$  in the correlation matrix the cosine between vectors  $\mathbf{T}_i$  and  $\mathbf{T}_j$ :

$$A_{ij} = \frac{\mathbf{T}_i \cdot \mathbf{T}_j}{|\mathbf{T}_i||\mathbf{T}_j|} = \frac{\sum_k T_{ik}T_{jk}}{\sqrt{\sum_k T_{ik}^2}\sqrt{\sum_k T_{jk}^2}} \quad (\text{S1})$$

As a result we obtain a square symmetric correlation matrix  $A$  with  $R$  rows/columns.

### Ordering the correlation matrix

The goal of this procedure is to order the rows/columns in such a way that variables (experimental conditions/observables) with the higher correlation are closest in the ordering (contiguous or close-to-contiguous rows/columns). This is analogous to finding the ordering for which the largest elements in the affinity matrix  $A_{ij}$  are closest to the diagonal. To find an ordering close to the optimal ordering, we use simulated annealing<sup>2</sup> with a cost function  $C$  that assigns to each element a weight equal to its distance to the diagonal:

$$C = \frac{1}{N} \sum_{i,j=1}^N A_{ij}|i-j| \quad (\text{S2})$$

where  $N$  is the number of rows/columns of the correlation matrix.

We start from a random initial ordering at temperature  $T$  (typically  $T \simeq 10$ ). For every iteration in the simulated annealing search, we propose  $\mathcal{O}(N^\epsilon)$  moves in which segments of contiguous rows attempt to change positions in the ordering. We accept or reject each attempted move following a standard Metropolis algorithm. For each attempt, we randomly pick: (a) a segment of contiguous rows and (b) a new position for the first row—the remaining rows will be placed keeping the relative distance to the first one. We pick the first row and its new position from a uniform distribution. We pick the width of the segment from a Gaussian distribution whose variance depends linearly on both the temperature  $T$  and the size of the matrix  $N$  so that for low temperatures only changes of single rows are proposed. We compute the value of the cost function for the new order  $C'$  and we accept the change with probability  $p = \exp[(C - C')/T]$ . After every iteration, we decrease the temperature by a factor in the range  $[0.95, 0.9999]$ . The process stops when  $C$  has not changed for 20 iterations.

### Cluster identification

To identify the best partition of the rows/columns into clusters, we assume the following structure for the correlation matrix: The ordered matrix has a block-diagonal structure with  $n$  boxes bound by  $n - 1$  breaking points  $b_s$ ,  $s = 2, \dots, n$ ;  $b_1 = 1$ . We assume that all matrix elements inside each box  $s$  are equal to  $A_s$  (in general  $A_s \neq A_{s'}$ ;  $s \neq s'$ ) and that all the elements outside the boxes along the diagonal are equal to  $B$ .

Our goal is to find the set of parameters  $\{n, b_2, \dots, b_n, B, A_1, \dots, A_n\}$  that best fits the data. We quantify the closeness-of-fit of a given set of parameters by the sum  $\mathcal{L}$  of the squared deviations of the data to the model

$$\mathcal{L} = \sum_{s=1}^n \sum_{(i,j) \in \mathcal{S}} (A_{ij} - A_s)^2 + \sum_{(i,j) \notin \mathcal{S}} (A_{ij} - B)^2 \quad (\text{S3})$$

where  $\mathcal{S}$  is the set of elements belonging to the diagonal boxes and the last sum runs over all matrix elements that do not belong to  $\mathcal{S}$ .

For a given set  $(n, b_1, \dots, b_n)$  the best estimators for  $(B, A_1, \dots, A_n)$  are:

$$A_s^* = \sum_{(i,j) \in \mathcal{S}} \frac{A_{ij}}{N_s} \quad \text{where} \quad N_s = \sum_{(i,j) \in \mathcal{S}} 1 \quad \text{for } s = 1, \dots, n \quad (\text{S4})$$

$$B^* = \sum_{(i,j) \notin \mathcal{S}} \frac{A_{ij}}{N_B} \quad \text{where} \quad N_B = \sum_{(i,j) \notin \mathcal{S}} 1 \quad (\text{S5})$$

To find a solution to this problem we use a greedy algorithm for partitioning the matrix. Specifically, we start by setting  $n = 1$  and by computing  $\mathcal{L}_1$  for a single box. Next, we assume  $n = 2$ , we calculate  $\mathcal{L}$  for  $b_2 = 2, \dots, N-1$ . We place the breaking point at the value of  $b_2$  for which  $\mathcal{L}$  is the smallest and we set  $\mathcal{L}_2 = \mathcal{L}$ .

We then consider the case  $n = 3$ . We do not consider all possible partitions of the matrix into three boxes but only those in which there are already two breaking points defined by  $(b_1, b_2)$ . We select the new breaking point as the value of  $b_3$  such that  $\mathcal{L}$  is minimum, and set  $\mathcal{L}_3 = \mathcal{L}$ . In practice, a rule of thumb to find a global minimum of  $\mathcal{L}$  is to keep iterating the same process as long as  $\mathcal{L}_n \simeq \mathcal{L}_{n-1}$ .

Note that the model that gives the minimum  $\mathcal{L}$  is likely to overfit the data because we are not taking into account the number of parameters in the model. Therefore, to select the best model we use the Bayesian information criterion (BIC)<sup>3</sup> which when using least-squares minimization reads as:

$$BIC = m * \ln\left(\frac{\mathcal{L}}{m}\right) + k \ln(m) \quad m = N^2 \quad (\text{S6})$$

where  $k$  is the number of parameters in the model. Our best model (that is, partition of the rows into clusters) is then the one for which the BIC is minimum.

## 2) Choice of physical properties and averaging

Our aim was to select a minimal subset of physical properties that captured meaningfully traction force, monolayer tension, cell velocity, and deformation rate. To select this subset from the large pool of measured physical properties (Table 1) we prioritized vectorial and tensorial components in the direction of cell expansion (maps of all other components are provided in Supplementary Note Figure 1) and avoided expectable correlations (see below for the analysis of correlations between different measures of cell velocity). Here we describe each of the variables chosen for our statistical analysis and we indicate how such variables were averaged over space, time, and experimental repeats.

- $\Delta A$ : Difference between final and initial monolayer area.  $\Delta A$  was measured by user-assisted thresholding.  $\Delta A$  was reported as the mean across experimental repeats.
- $V_x$ : Instantaneous velocity along the  $x$ -axis measured using PIV. Given the axial symmetry of monolayer expansion, the average of  $V_x$  is roughly zero. We thus report the median of  $|V_x|$  (i.e. the unsigned value of  $V_x$ ) of each map, and averaged all map medians over time and experimental repeats.
- $\dot{\varepsilon}_{xx}$ : Strain rate in the direction of tissue expansion. The strain rate (or deformation rate) is a 2D tensor  $\dot{\boldsymbol{\varepsilon}}$  that describes the rate of change of the deformation of the monolayer at any given point in space and moment in time. The tensor comprises 2 normal components ( $\dot{\varepsilon}_{xx}$  and  $\dot{\varepsilon}_{yy}$ ) and two shear components ( $\dot{\varepsilon}_{xy}$  and  $\dot{\varepsilon}_{yx}$ ):

$$\dot{\boldsymbol{\varepsilon}} = \begin{pmatrix} \dot{\varepsilon}_{xx} & \dot{\varepsilon}_{xy} \\ \dot{\varepsilon}_{yx} & \dot{\varepsilon}_{yy} \end{pmatrix} \quad (\text{S7})$$

Here we focused on the normal component along the  $x$ -axis, and computed it using a continuum approximation<sup>4</sup>:

$$\dot{\varepsilon}_{xx} = \frac{dV_x}{dx} \quad (\text{S8})$$

To report  $\dot{\varepsilon}_{xx}$  we computed the median of each map, and then the mean of all map medians over time and experimental repeats.

- $U$ : Strain energy of a monolayer.  $U$  measures the mechanical energy transferred by the monolayer to the underlying gel. It was computed from the traction vectors  $\vec{T}$  and the displacement vectors  $\vec{u}$  as <sup>5</sup>:

$$U = \frac{1}{2} \iint \vec{T} \cdot \vec{u} dx dy \quad (\text{S9})$$

$U$  was computed for each time point and reported as the mean over time across experimental repeats.  $U$  showed a strong correlation with other common measures of traction forces, such as the total traction (sum of  $|\vec{T}|$  over space, time, and experimental repeats). In an elastic material,  $U$  and  $\Delta A$  are correlated. The absence of correlation found in our study highlights that frictional losses dominate in the time scales and knock-down conditions of our study.

- $\sigma_{xx}$ : Monolayer tension or intercellular tension in the direction of monolayer expansion. The state of mechanical stress at any point of a 2D monolayer is fully determined by the stress tensor  $\sigma$ :

$$\sigma = \begin{pmatrix} \sigma_{xx} & \sigma_{xy} \\ \sigma_{yx} & \sigma_{yy} \end{pmatrix} \quad (\text{S10})$$

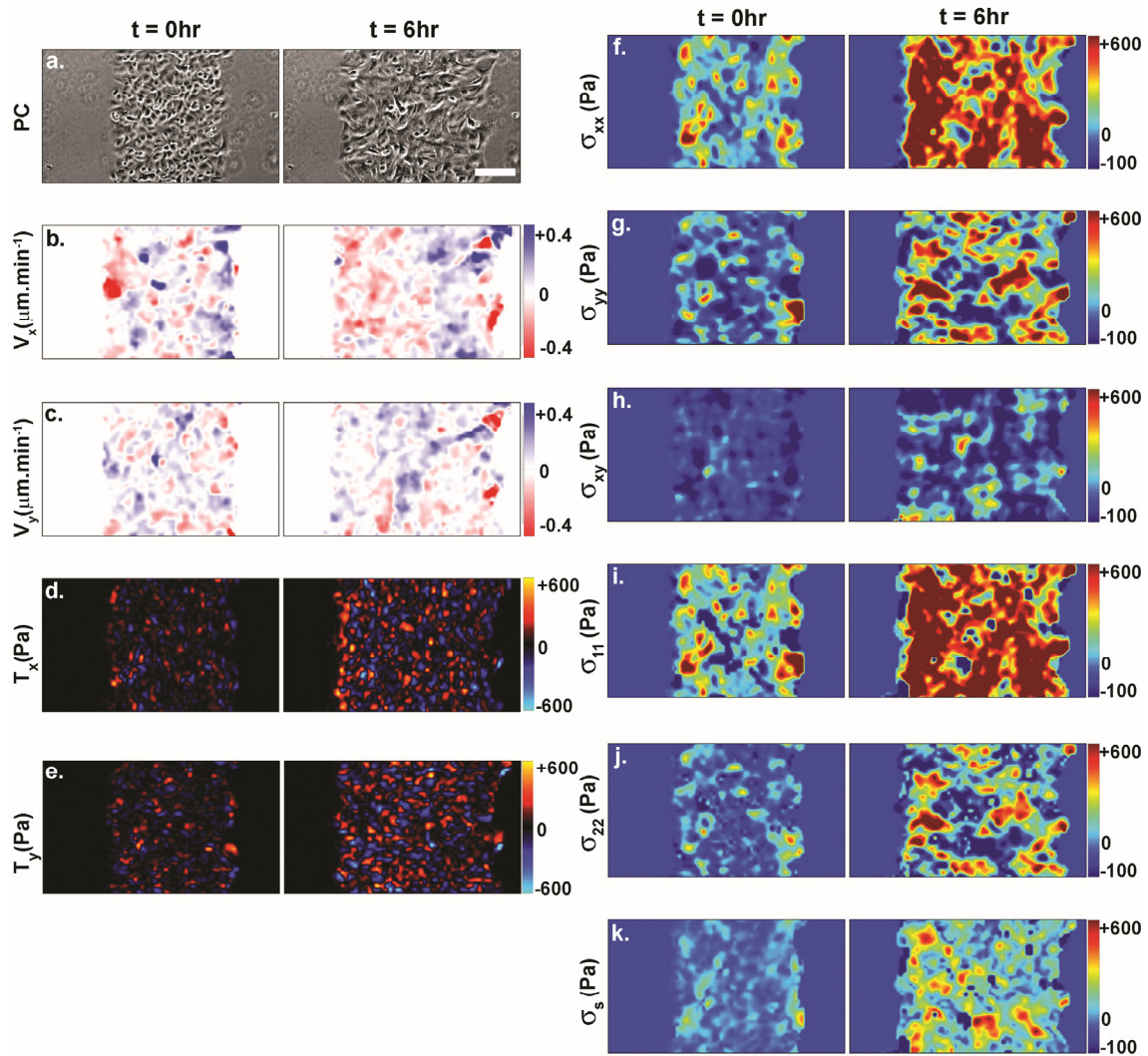
where  $\sigma_{xx}$  and  $\sigma_{yy}$  are normal stress components, and  $\sigma_{xy}$  and  $\sigma_{yx}$  are shear stress components. The four components of the stress tensor define two particular directions at every point of the monolayer. These directions, which are mutually orthogonal, are called principal stress orientations, and the stress values in each principal orientation are called maximum ( $\sigma_{11}$ ) and minimum ( $\sigma_{22}$ ) principal stress components. From the principal stress components, the average normal stress is defined as  $\sigma_n = (\sigma_{11} + \sigma_{22})/2$ . In our experiments, we found that  $\sigma_n$ ,  $\sigma_{11}$  and  $\sigma_{xx}$  were highly correlated across siRNA perturbations. As such, we chose to use solely  $\sigma_{xx}$  for our statistical analysis. To report  $\sigma_{xx}$  we computed the median of each map, and then the mean of all map medians across experimental repeats. The mean of this quantity over time was termed  $\sigma_{xx}^m$  and the value of  $\sigma_{xx}$  at the end of the experiment was termed  $\sigma_{xx}^f$ .

- $\sigma_s$ : The maximum shear stress was defined as  $\sigma_s = (\sigma_{11} - \sigma_{22})/2$ . In addition to reporting the maximum value of the shear stress at each point of the monolayer,  $\sigma_s$  is an indicator of tension anisotropy. To report  $\sigma_s$  we computed the median of each map, and then the mean of all map medians over time and experimental repeats.
- $\dot{\sigma}_{xx}$ : To capture the time evolution of monolayer tension, we fitted a linear polynomial to  $\sigma_{xx}$ :

$$\sigma_{xx}(t) = \dot{\sigma}_{xx}t + \sigma_0 \quad (\text{S11})$$

where  $t$  indicates time. To report  $\dot{\sigma}_{xx}$  we fitted Eq. S11 to each experiment and then computed the mean of  $\dot{\sigma}_{xx}$  over experimental repeats.



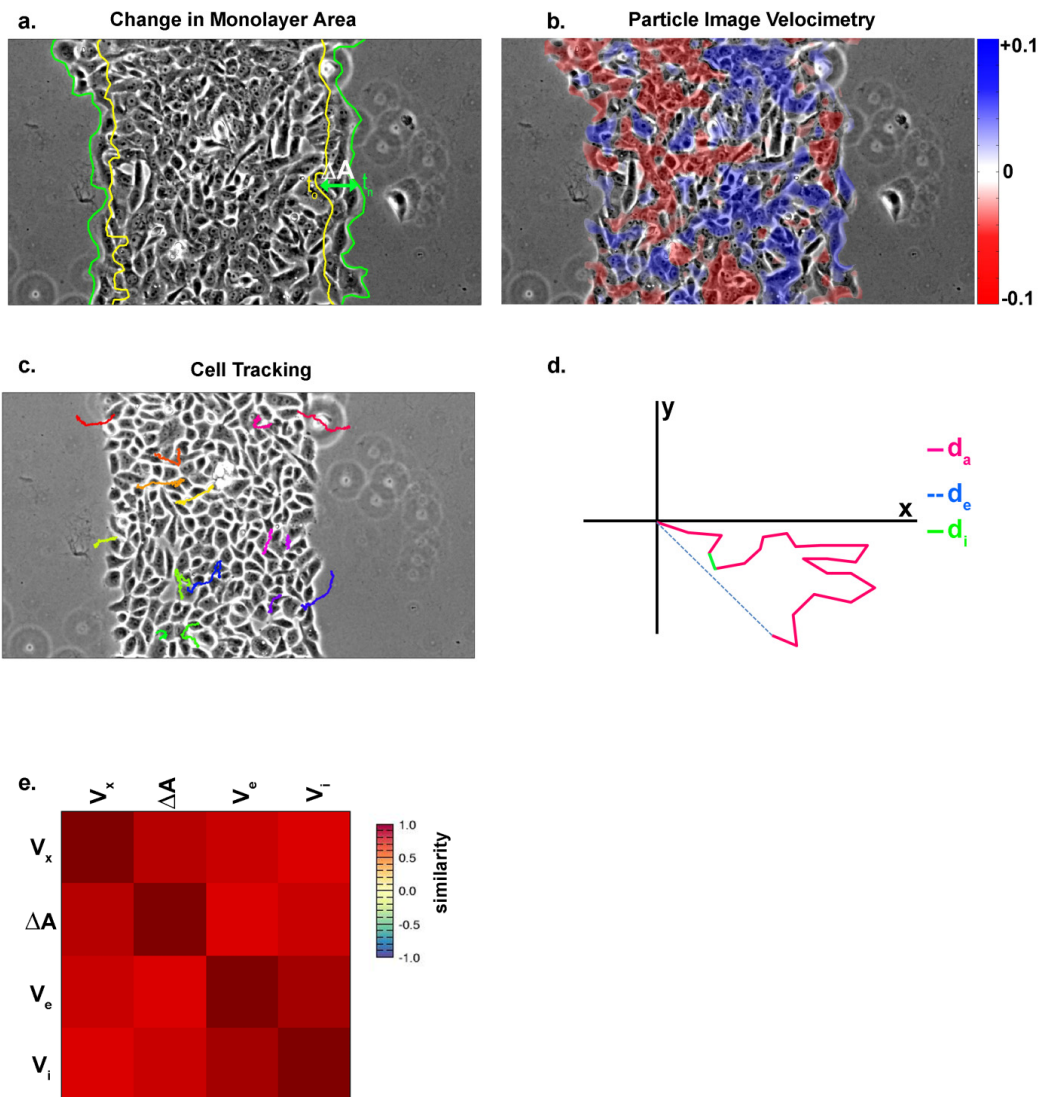


**Supplementary Note Figure 1. Representative maps of force components at the onset of monolayer expansion (left panels) and 6 hours later (right panels).** (a) phase contrast, (b) velocity in the  $x$  direction, (c) velocity in the  $y$  direction, (d) traction forces in the  $x$  direction, (e) traction forces in the  $y$  direction, (f) normal component of the monolayer stress tensor in the  $x$  direction, (g) normal component of the monolayer stress tensor in the  $y$  direction, (h) monolayer shear stress component, (i) maximum principal stress in the monolayer, (j) minimum principal stress in the monolayer, (k) maximum shear stress in the monolayer. Scale bar,  $100\mu\text{m}$ .

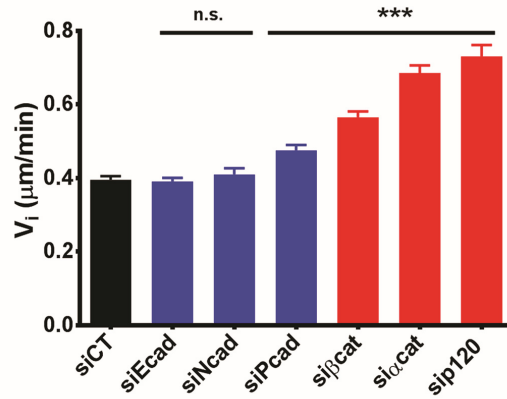
### 3) Correlation between measures of cellular kinematics

To fully capture monolayer kinematics we used three different techniques. Firstly, we measured monolayer expansion by computing the change in monolayer area ( $\Delta A$ ) between the beginning and the end of the experiment (360 min) (Supplementary Note Figure 2a). Secondly, we mapped the instantaneous local velocity ( $V_x, V_y$ ) everywhere in the cell monolayer using Particle Imaging Velocimetry (Supplementary Note Figure 2b). Thirdly, for each siRNA perturbation we tracked 60 cells randomly distributed in the monolayer (Supplementary Note Figure 2c). For each cellular track we obtained the instantaneous cell velocity ( $V_i$ , velocity between two consecutive time points) and the Euclidian velocity ( $V_e$ , Euclidian distance between the initial and final cell positions divided by the recording time) (Supplementary Note Figure 2d). Once averaged across space and experimental repeats, some of the quantities described above are expected to show some degree of correlation but this need not be the general case. For example, cells restricted to patterns would exhibit no change in area but a significant velocity field, and this velocity field might be persistent or random. Measurements of cellular kinematics based on the three different techniques yielded consistent results. For example, they all showed that knocking down P-cadherin (but not E-cadherin or N-cadherin) and catenins resulted in a significant increase in kinematic quantities (Supplementary Note Figure 3).

To assess systematically the agreement between different kinematic measures we computed the correlation matrix (see methods) between  $V_x$ ,  $\Delta A$ ,  $V_i$ , and  $V_e$ . This matrix shows that all measures of cellular kinematics are highly correlated (Supplementary Note Figure 2e). Given such correlation, we chose to use  $V_x$  and  $\Delta A$  for our global analysis of cellular kinematics.



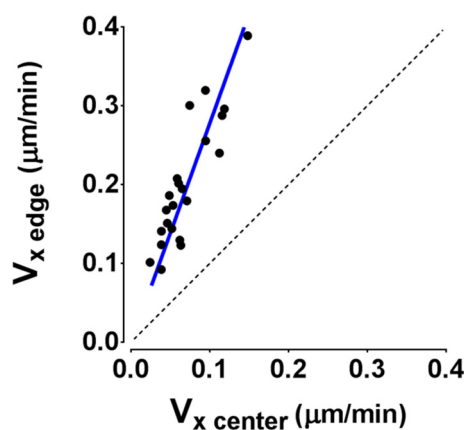
**Supplementary Note Figure 2. Different measures of cellular kinematics are highly correlated.** Methods to assess cellular kinematics include a) change in monolayer area, b) PIV, c-d) cell tracking. For each cell track we measured the average distance travelled between two acquisition time points ( $d_i$ ) and the Euclidian distance between the initial and final time points ( $d_e$ ). From these distances we obtained  $V_i$  and  $V_e$ . e) Correlation matrix (cosine similarity) between all measures of cell velocity.



**Supplementary Note Figure 3. Effect knocking down cadherins and catenins on cell velocity.** siRNAs targeting E-cadherin and N-cadherin did not affect cell velocity. By contrast, siRNAs targeting P-cadherin,  $\alpha$ -catenin,  $\beta$ -catenin, and p120 increased cell velocity significantly (n=60 cells per condition, \*\*\* indicates  $p < 0.001$  compared to control using Student's t-test, n.s. indicates  $p > 0.05$ ).

#### 4) Cellular velocity at the Edge vs Center of the monolayer

Averaging over space necessarily implies a loss of information. For example, our analysis based on spatial averages might hide systematic differences between cell velocities in the monolayer center and edge. To study this possibility we divided the monolayer in two regions, a boundary band of 64  $\mu\text{m}$  width (first 2 rows of cells at each edge) and the remaining central region. We then compared average velocities in those two regions. This analysis revealed that cellular velocities at the center of the monolayer were systematically smaller than those at the edge, but both velocities scaled linearly across siRNA perturbations (Supplementary Note Figure 4).

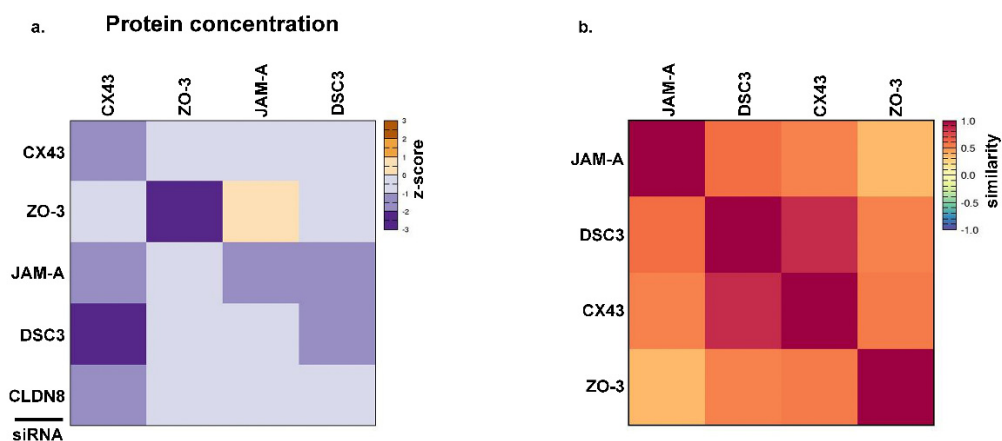


**Supplementary Note Figure 4. Velocity at the edge vs center of the monolayer.** Each data point corresponds to one siRNA perturbation. The blue line is a linear fit with zero intercept. The dashed line is the identity line.

## 5) Co-regulation within mechanical modules

Our measurements of protein concentrations within the Fast/Weak module show strong co-regulation (main Fig. 6). Here we analyze whether proteins comprising the Steady/Weak module are also co-regulated. Unlike the case of the Fast/Weak module, which includes all proteins from adherens junctions, the Steady/Weak module includes proteins from tight junctions (CLDN8, ZO-3, JAM-A), gap junctions (CX43), and desmosomes (DSC3). To study whether these seemingly unrelated proteins exhibit co-regulation patterns we measured protein concentrations of ZO-3, JAM-A, CX43, and DSC3 in cells treated with CT siRNA, CLDN8 siRNA, ZO-3 siRNA, JAM-A siRNA, CX43 siRNA, and DSC3 siRNA (see Methods). For each experiment we computed the matrix of z-scores (Supplementary Note Figure 5a) and the corresponding correlation matrix (Supplementary Note Figure 5b).

These experiments unveil co-regulation events within the Steady/Weak module. Nearly all siRNA caused a drop in all protein concentrations within the module (with the exception of JAM-A under siZO-3, Supplementary Note Figure 5). This was particularly pronounced in the case of CX43 under DSC3 siRNA. Analysis of the correlation matrix showed that the levels of expression of all proteins within the Steady/Weak were positively correlated when subjected to siRNA perturbations, with DSC3 and CX43 showing the strongest co-regulation. Together with our analysis of Fig. 6, these findings establish that proteins that comprise mechanical modules show similar patterns of expression.



**Supplementary Note Figure 5. Co-regulation between proteins comprising the Steady/Weak cluster.** a) z-scores of protein concentrations for ZO-3, JAM-A, CX43, and DSC3 in cells treated with CLDN8 siRNA, ZO-3 siRNA, JAM-A siRNA, CX43 siRNA, and DSC3 siRNA. b) Correlation between protein expression patterns computed as the cosine similarity between columns in panel (a).

## 6) A linear combination of cadherin and catenin concentrations is a significant predictor of intercellular forces

Our analysis in Fig. 6 showed that the concentration of P- or E-cadherin alone is sufficient to predict significantly intercellular tension and its time evolution. We next asked whether a combination of protein concentrations is a better predictor of monolayer mechanics than a single protein concentration. As the simplest model involving multiple proteins, we assumed that any given physical property  $X_j$  can be predicted by a linear combination of the concentrations of  $N$  proteins ( $N=2-8$ ):

$$X_j = A + \sum_{i=1}^N B_i [p_i] \quad (\text{S12})$$

To test the predictive power of each combination, we conducted again a LOOCV analysis. We note that a cross-validation analysis is conceptually distinct from a simple linear fit; while adding more parameters to a model always implies a better fit, it does not necessarily imply higher predictive power (in fact, it often leads to lower predictive power due to overfitting).

Similarly to the case of one-protein models, N-protein models were largely unable to predict cell velocities, cell deformations, and cell tractions. By contrast, several linear combinations of multiple protein concentrations were predictive of average intercellular tension, intercellular tension at the end of the experiment, and intercellular tension buildup rate (Supplementary Table 3). These linear combinations, which led to smaller prediction errors than one-protein models, always included at least one cadherin, but sometimes the three of them. In addition, they generally involved  $\beta$ -catenin,  $\alpha$ -catenin, or p120. The large number of N-protein models that were found to predict intercellular tension and its buildup rate highlights the fact that proteins comprising adherens junctions are co-regulated. Neither ZO-1 nor occludin appeared in any of the significant models of intercellular tension magnitude or rate, indicating that these proteins are not involved in the control of these physical properties.

## **Supplementary References**

1. Sales-Pardo, M., Guimera, R., Moreira, A.A. & Amaral, L.A. Extracting the hierarchical organization of complex systems. *Proc Natl Acad Sci U S A* **104**, 15224-15229 (2007).
2. Kirkpatrick, S., Gelatt, C.D. & Vecchi, M.P. Optimization by Simulated Annealing. *Science* **220**, 671-680 (1983).
3. Schwarz, G. Estimating the Dimension of a Model. *Ann Statist* **6** 461-464 (1978).
4. Serra-Picamal, X. *et al.* Mechanical waves during tissue expansion. *Nature Physics* **8**, 628-634 (2012).
5. Butler, J.P., Tolic-Norrelykke, I.M., Fabry, B. & Fredberg, J.J. Traction fields, moments, and strain energy that cells exert on their surroundings. *American journal of physiology* **282**, C595-605 (2002).